Universidad Zaragoza
1542

Proyecto Fin de Carrera

Investigation of Variety of Non-Coherent Front end Detectors for Timing Estimation

Autor

Luis Lacasa Calvo

Director/Supervisor

Satyam Dwivedi

Ponente

Enrique Masgrau Gómez

Escuela de Ingeniería y Arquitectura

2013

Investigation of Variety of Non-Coherent Front End Detectors For Timing Estimation

Resumen

La localización en interiores de usuarios móviles es actualmente un tema central para muchas aplicaciones y campos, incluidas las redes de sensores, gestión de activos, asistencia sanitaria y localización de personal de seguridad pública. Las soluciones existentes se basan a menudo en la fusión de la información de múltiples sensores.

La posibilidad de utilizar un sistema de banda ultra ancha (UWB) para la medición inalámbrica de distancias basada en el tiempo de ida y vuelta (RTT) se ha investigado en este proyecto final de carrera. Los receptores UWB no coherentes se han analizado utilizando dos enfoques diferentes: la detección de la amplitud y la detección de la energía. Para el análisis, se desarrolla un estudio teórico y también se han realizado diversas simulaciones. Además, ambos receptores UWB no coherentes han sido diseñados e implementados. Por otra parte, un método ha sido propuesto para permitir la reconstrucción de un pulso UWB a partir del submuestreo de una ráfaga de pulsos UWB y tratar de aproximar el rendimiento óptimo del receptor UWB ideal.

Las simulaciones producen resultados interesantes en cuanto al rendimiento de la estimación de RTT. Ambas técnicas de detección se comparan, describiendo las ventajas y desventajas de cada uno.

Tabla de Contenidos

Capítulo 1

Introducción

En este Proyecto Final de Carrera se ha investigado el uso de sensores de banda ultra-ancha (UWB) para localización en interiores, basándose en la medida del tiempo de ida y vuelta (RTT) de pulsos UWB. Se analizan dos tipos diferentes de receptores no coherentes (detección de amplitud y detección de energía), para así averiguar las ventajas e inconvenientes de cada uno. Además, el receptor UWB ideal también es analizado para ser comparado con los receptores no coherentes. Los resultados que se presentan en esta memoria, podrían ser de gran ayuda en la implementación de sensores UWB para medida de distancias.

Esta memoria ofrece tanto análisis teórico como los resultados de las simulaciones llevadas a cabo durante el trabajo correspondiente a este PFC. Dichos resultados revelan características interesantes acerca del funcionamiento de los receptores UWB no coherentes. El principal objetivo es averiguar cuál de los receptores no coherentes estudiados presenta mejor rendimiento en determinadas situaciones. Además, distintas formas de los pulsos UWB son consideradas en el análisis.

En este PFC se han diseñado e implementado también los dos tipos de receptores mencionados anteriormente. Uno de los capítulos está orientado a la descripción de estos diseños. Los diseños están basados en una implementación anterior realizada en el laboratorio de procesado de señal de la universidad KTH de Estocolmo, la cual se detalla en [1].

Un método que trata de aproximar el rendimiento del receptor ideal se ha propuesto en este PFC. Se trata de reconstruir un pulso UWB usando submuestreo sobre un tren de pulsos. Este método no se ha diseñado ni simulado, simplemente es una idea que pudiera ser usada en futuras investigaciones.

1.1. Contexto

Este Proyecto Fin de Carrera ha sido realizado durante estudios de intercambio en la universidad KTH (Kungliga Tekniska Högskolan) de Estocolmo, Suecia; específicamente en el Laboratorio de Procesado de Señal de la EES (Electrical Engineering School). En dicho laboratorio, se implementó anteriormente a este trabajo un sistema UWB para medida de distancias. Dicha implementación está descrita en [1].

1.2. Motivación y Trabajo Previo

La localización en interiores de usuarios móviles es actualmente un tema central para muchas aplicaciones y campos, incluidas las redes de sensores, gestión de activos, la asistencia sanitaria, y localización de personal de seguridad pública [2]. Existen soluciones basadas el uso de múltiples sensores. En particular, algunos de los tipos de sensores más utilizados son los sistemas de navegación inercial [3], sistemas de imagen como cámaras o sensores infrarrojos [4], y tecnologías de posicionamiento basados en las radiocomunicaciones.

La medición de la posición de los usuarios con precisión y fiabilidad es de particular relevancia en escenarios de localización de organismos de respuesta inmediata (bomberos, paramédicos, etc.), donde el conocimiento de la ubicación en entornos de sistemas globales de navegación por satélite (GNSS) es una herramienta importante para la eficiencia y la seguridad [5]. En dichos escenarios, las soluciones se suelen basar en técnicas cooperativas y oportunistas, ya que el sistema proporcionado debe ser operativo incluso en la ausencia de una infraestructura de localización preinstalada.

Para investigar experimentalmente la medición de distancia y posición en interiores por medio de radiocomunicaciones, numerosos métodos han sido propuestos en la literatura. Sistemas como el descrito en [6] se implementan utilizando sistemas de comunicación inalámbrica de corto alcance. Además, para aplicaciones en las que no son estrictamente necesarias medidas muy precisas, es posible utilizar detectores de proximidad, tal como la técnica de detección de proximidad casi omnidireccional, basada en ZigBee descrita en [7].

En este contexto, los sistemas de banda ultra ancha (UWB) son objeto de considerable interés en la investigación, debido principalmente a su alta resolución y al bajo consumo de energía [8]. En particular, [9] propuso un nuevo nodo híbrido inalámbrico basado en el estándar radio tradicional IEEE802.15.4 con el apoyo de un transceptor UWB para la medida precisa de tiempo. Típicamente, una motivación de la utilización del sistema UWB en un sistema de localización multisensor es prevenir el crecimiento del error inherente a los sistemas de navegación inercial, porque el error en las estimaciones de distancia con UWB está limitado [10].

1.3. Planteamiento del Problema

Varios estudios han analizado la estimación del tiempo de llegada (TOA) usando sistemas UWB y muestreo, por ejemplo [11, 12]. Tales métodos requieren sincronización, y además, el extremadamente amplio ancho de banda de los pulsos UWB hace muy complejo el muestreo utilizando la frecuencia de muestreo de Nyquist. Por lo tanto, en este PFC se investigan los receptores UWB no coherentes. El RTT se utiliza para la medición de la distancia en lugar del TOA, por lo tanto no se necesita sincronización entre sensores.

El desarrollo del sensor descrito en esta tesis sigue un enfoque novedoso que combina varios aspectos clave:

- Medida de distancia basada en tiempo de ida y vuelta
- Énfasis en las capacidades del procesado digital de señal
- Funcionamiento asíncrono
- Alta tasa de actualización de la medición
- Diseño basado en conversor tiempo-digital

Estas características hacen que el sensor sea especialmente adecuado para la investigación experimental para aplicaciones de localización de interiores para organismos de respuesta inmediata (bomberos, paramédicos, etc.), sobre todo porque el tiempo de ida y vuelta no necesita de una infraestructura preinstalada y el TDC permite lograr alta precisión en la medida con baja complejidad y bajo consumo.

1.3.1. Tipos de receptores UWB no coherentes

En este PFC se han considerado para el estudio dos tipos de receptores UWB no coherentes: detección de energía y detección de amplitud.

Detección de energía La técnica detección de energía (ED) es ampliamente estudiada en la literatura de UWB. La detección del pulso se realiza comparando la energía de la señal recibida con un umbral.

Detección de amplitud En este caso, la propia amplitud se compara directamente con un umbral. La detección de amplitud no ha sido tan estudiada en la literatura, pero aunque su rendimiento es a priori peor que el de ED, es interesante su estudio y como se mostrará en las simulaciones presentadas en el capítulo 5, puede ser adecuado su uso en determinadas situaciones.

1.3.2. Objetivo principal de este PFC

En este PFC se ha tratado de averiguar cómo afectan y cuáles son los principales aspectos que afectan al rendimiento de la medición de de tiempos de ida y vuelta de pulsos UWB para estimar distancias usando receptores UWB no coherentes; para así seleccionar la configuración más adecuada (tipo de receptor, forma de onda del pulso UWB, umbral, etc) para unas ciertas condiciones.

1.4. Organización de la Memoria

Esta memoria es una síntesis en español de la memoria original y completa en inglés, la cual está incluida en el Apéndice A. Se ha tratado de hacer dicha síntesis lo más autocontenida posible y debería ser suficiente para extraer los aspectos fundamentales de este PFC. Sin embargo, no todo está incluido y por ello, se recomienda también leer la versión completa del apéndice. Tanto la versión en castellano como en inglés, están divididas en capítulos (iguales en ambas versiones), cuyos contenidos se detallan a continuación.

El segundo capítulo trata sobre los principios básicos de las señales UWB, así como el receptor UWB ideal. Se describen distintas formas de pulsos UWB. Además, se analiza teóricamente el receptor UWB ideal.

El capítulo 3 describe los dos tipos de receptores UWB no coherentes, detección por amplitud y por energía. Está dedicado a presentar los principios básicos y teoría relacionados con los sistemas que han sido investigados y simulados en este PFC.

El siguiente capítulo, presenta el diseño del hardware de los receptores UWB no coherentes descritos en el anterior capítulo. Estos diseños están basados en el trabajo previo realizado en el laboratorio de procesado de señal de la KTH. Se proporciona una lista con los componentes usados en dichos diseños.

El quinto capítulo está dedicado a la presentación de los resultados de las simulaciones llevadas a cabo durante este PFC. De esta manera, se compara el rendimiento de las dos técnicas de detección investigadas, así como de las distintas formas de pulso consideradas. Los resultados son interesantes y podrían resultar de ayuda en futuras investigaciones o desarrollo de sensores UWB.

El capítulo 6 presenta el método propuesto en este PFC para estimación de distancias basado en el submuestreo de señales UWB.

Finalmente, el último capítulo concluye esta memoria con una discusión y comentarios acerca la posible continuación del trabajo desarrollado. Todas las referencias a estudios previos se encuentran al final de la memoria en la Bibliografía.

A continuación de la versión en castellano de la memoria se encuentra la versión original escrita en inglés.

Capítulo 2

Señales UWB y Receptor Ideal

En este capítulo el lector obtendrá conceptos básicos de los sistemas UWB. Las distintas formas de los pulsos que han sido consideradas se presentan en la sección 2.1 y la sección 2.2 describe el receptor UWB ideal.

Desde un punto de vista regulatorio, un sistema UWB es definido en [13] como cualquier sistema radio con un ancho de banda fraccional mayor que el 20 % o un ancho de banda absoluto mayor que 500 MHz. Además, máscaras espectrales que definen los límites superiores de las emisiones son proporcionados por agencias de regulación; véase por ejemplo, [13, 14].

2.1. Formas de Pulsos UWB

Esta sección presenta las distintas formas de onda de pulsos UWB que han sido consideradas en este PFC, las cuales se describen en [15]. En la Figura 2.1 se muestran las formas de onda de todos los pulsos. Por otro lado, en la Tabla 2.1 se muestran valores numéricos de la energía de cada pulso, así como los anchos de banda. Como puede observarse, para la misma amplitud, los distintos tipos de pulso tienen distinta energía, lo cual influirá en el rendimiento del método de detección de amplitud. La energía de un pulso puede expresarse como $E_b = k_s T_b A^2$, donde T_b es la duración del pulso, A es la amplitud y k_s es un parámetro característico de cada pulso (con $0 \leq k_s \leq 1$).

Las expresiones matemáticas que describen cada pulso pueden encontrarse en esta misma sección de la versión original en el apéndice A.

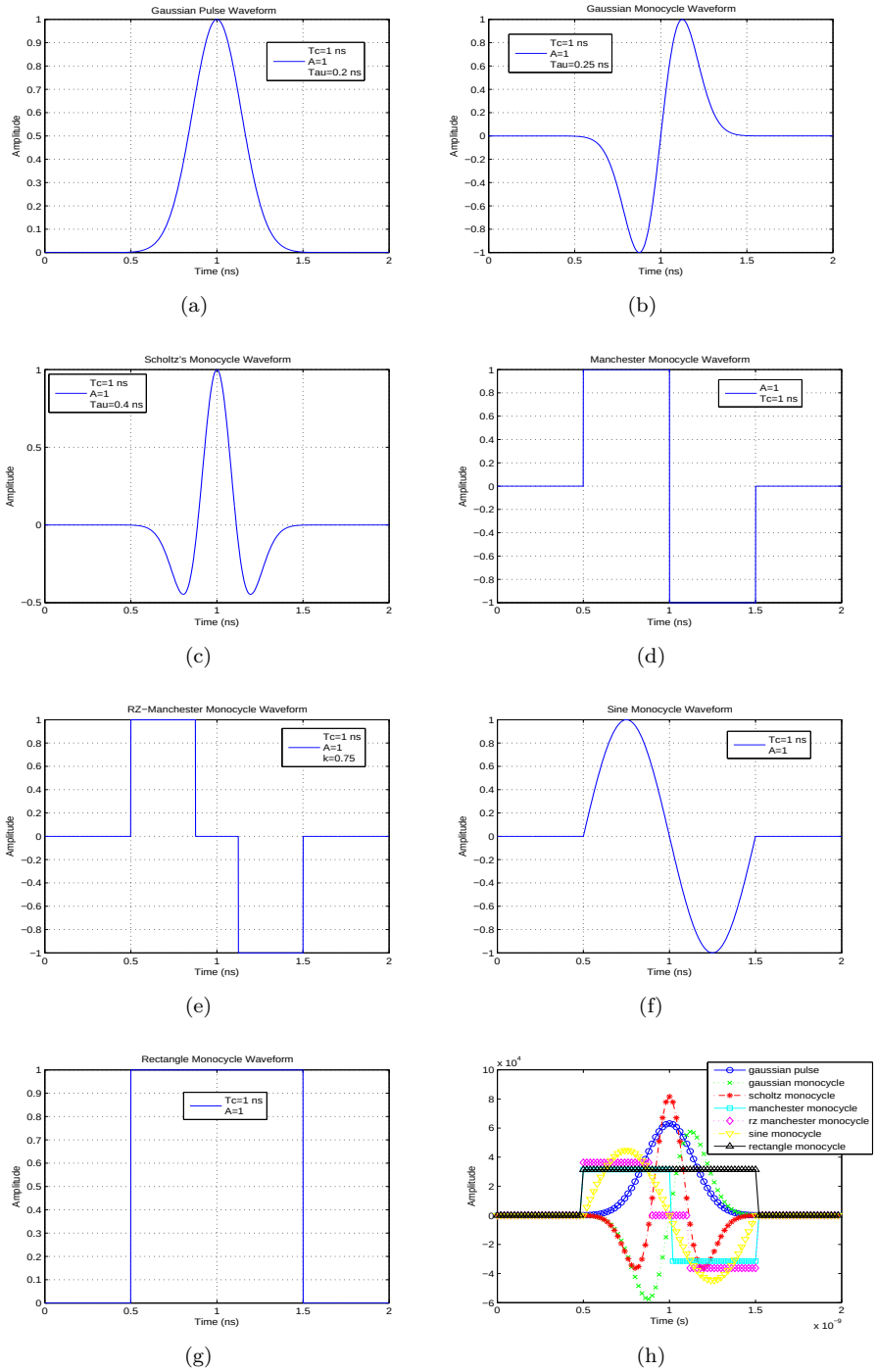

Figure 2.1: Formas de onda de los pulsos con duración $T_b = 1\,ns$: (a) pulso Gaussiano, (b) monociclo Gaussiano , (c) monociclo de Scholtz, (d) monociclo Manchester, (e) monociclo RZ-Manchester, (f) monociclo sinusoidal, (g) monociclo rectangular, y (h) todas las formas juntas con la misma energía.

Tabla 2.1: Energía de cada forma de pulso en función de la amplitud y ancho de banda a 3 dB.

Forma de pulso	Energía en función de A	Ancho de banda a 3 dB
Pulso Gaussiano	$2{,}5066 \cdot 10^{-10} \cdot A^2$	0 - 1 GHz
Monociclo Gaussiano	$3{,}0113 \cdot 10^{-10} \cdot A^2$	500 MHz - 1.5 GHz
Monociclo de Scholtz	$1{,}5 \cdot 10^{-10} \cdot A^2$	1 GHz - 2.3 GHz
Monociclo Manchester	$10^{-9} \cdot A^2$	300 MHz - 1.2 GHz
Monociclo RZ-Manchester	$k \cdot 10^{-9} \cdot A^2$	500 MHz - 1.4 GHz
Monociclo sinusoidal	$5 \cdot 10^{-10} \cdot A^2$	400 MHz - 1.3 GHz
Monociclo rectangular	$10^{-9} \cdot A^2$	0 - 1 GHz

2.2. Receptor UWB Ideal

Aunque el principal objetivo de este PFC no es investigar el receptor ideal, puede ser interesante analizarlo para así compararlo con los receptores no coherentes. Dicho receptor ideal se basa en la suposición de que es posible muestrear los pulsos UWB con una tasa de muestreo superior a la de Nyquist. Dado que el ancho de banda es muy amplio, dicha tasa de muestreo sería muy alta, y por lo tanto el diseño puede llegar a ser muy complejo e incluso inviable en muchos casos.

Asumiendo que es posible realizar el sobremuestreo, la señal recibida puede ser correlada con la forma de onda del pulso. La señal UWB recibida tras filtrado y amplificación puede ser expresada como

$$r(t) = \sqrt{E_b} p(t - t_d) + n(t) \tag{2.1}$$

donde E_b es la energía del pulso tras amplificación y t_d representa un retraso genérico. El pulso UWB con energía unitaria y retraso nulo (empieza en $t = 0$) se denota por $p(t)$. El ruido aditivo, blanco y Gaussiano (AWGN) con media nula y densidad espectral de potencia $\frac{\mathcal{N}_0}{2}$ se representa por $n(t)$. La varianza o potencia del ruido es $\sigma^2 = \mathcal{N}_0 \cdot B$, siendo B el ancho de banda del filtro. Por simplicidad, se asume que el ancho de banda de la señal UWB es T_b^{-1} y que es paso-bajo. De esta forma, $B = T_b^{-1}$. La relación señal a ruido (SNR) se define como

$$SNR = \frac{E_b}{\mathcal{N}_0} \tag{2.2}$$

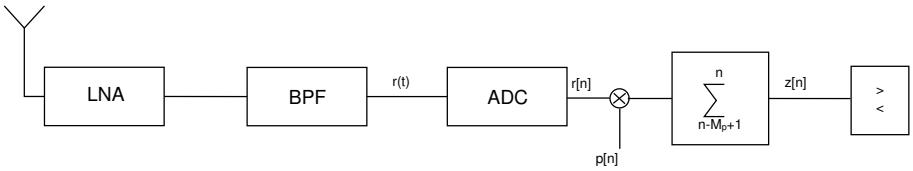

Figure 2.2: Diagrama de bloques del receptor UWB ideal.

El diagrama de bloques de este receptor ideal se muestra en la Figure 2.2 . La correlación de la señal recibida con el pulso se puede expresar como

$$z\left[n\right] = \sum_{k=n-M_p+1}^{n} r\left[k\right] p\left[k-n+M_p-1\right] \tag{2.3}$$

siendo M_p el número de muestras que contiene un pulso ($M_p = \frac{T_b}{t_s}$), con t_s representando el tiempo entre muestras ($f_s = t_s^{-1}$). La señal correlada se compara con un umbral, γ, para detectar el pulso. Es decir, cuando $z\left[n\right]$ cruza el umbral, el detector estima que el pulso está presente. Dicho umbral puede ser fijado como una fracción de $\sqrt{E_b}$, ya que es el máximo que alcanza la señal correlada sin considerar el ruido.

$$\gamma = k\sqrt{E_b}\,; 0 \leq k \leq 1 \tag{2.4}$$

Capítulo 3

Receptores UWB no coherentes

Ya que el uso del receptor UWB ideal (véase 2.2) es complejo o incluso inviable, nos interesa un diseño más simple. Dos técnicas de detección no coherente son investigadas en este PFC: detección de amplitud y detección de energía. Tales técnicas se implementan en el dominio analógico, por lo que no es necesario muestrear la señal recibida, siendo de esta forma el diseño mucho más simple.

Los receptores no coherentes no requieren estimación de canal y su implementación se de baja complejidad, a costa de una pérdida de rendimiento. Los receptores subóptimos no coherentes son adecuados para escenarios de baja potencia y bajo coste. Estos receptores no requieren sincronización, por lo que no es necesaria una infraestructura preinstalada. La detección se realiza simplemente comparando alguna característica de la señal UWB recibida (amplitud o energía en nuestro caso) con un umbral, siendo la implementación completamente analógica.

3.1. Arquitectura del los receptores no coherentes

Dos tipos diferentes de receptores UWB no coherentes se estudian en este PFC. Lo único que cambia entre ellos es la técnica con la que se detectan los pulsos. En ambos la señal recibida es filtrada y amplificada, tras lo cual cada uno es diferente:

- **Detección de amplitud**: La amplitud de la señal recibida se compara con un umbral, es decir, sólo se necesita un comparador.
- **Detección de energía**: En este caso se calcula la energía de la señal recibida en un intervalo de tiempo T_I y se compara con un umbral. Se necesita un dispositivo cuadrático y un integrador para calcular la energía, además de un comparador como en el caso de detección de amplitud.

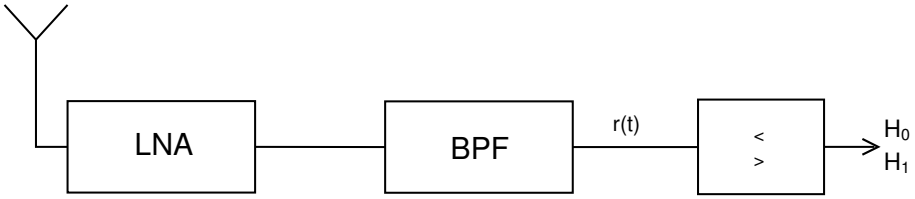

Figura 3.1: Diagrama de bloques del receptor UWB no coherente con detección de amplitud.

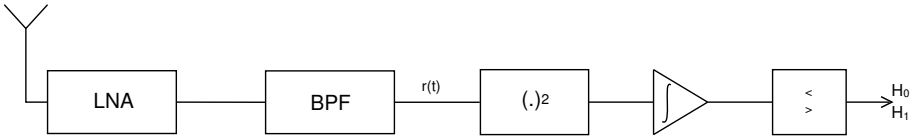

Figura 3.2: Diagrama de bloques del receptor UWB no coherente con detección de energía.

Los diagramas de bloques de estos receptores no coherentes se ilustran en las Figuras 3.1 (amplitud) y 3.2 (energía). El diseño del hardware se describirá en el capítulo 4.

3.2. Procedimiento de medida de la distancia

El objetivo es estimar el tiempo de ida y vuelta (RTT) de un pulso UWB que se propaga entre dos sensores; denominados como maestro y esclavo. El maestro es el que realmente mide la distancia y controla el procedimiento de la medida, mientras que el esclavo se encuentra en modo de espera hasta que detecta la llegada de un pulso, y entonces le responde al maestro con otro pulso. Los dos sensores están diseñados con el mismo receptor no coherente.

La distancia se mide repetidamente con una tasa de actualización denotada por R_f. En este contexto, una tasa de actualización de la medida de al menos 100 Hz es deseable para un seguimiento de la distancia con alto y preciso rango dinámico. El inverso de R_f se denota como T_f y representa la duración de una trama. En este documento una trama se define como el intervalo de tiempo en el cual el maestro realiza una medición de distancia. De esta forma, el procedimiento de medida se repite en cada trama y sigue los siguientes pasos:

1. El maestro inicia el procedimiento de medida mediante la transmisión de un pulso UWB. Se transmite un pulso al comienzo de cada trama.

2. Cuando el esclavo detecta el pulso, éste responde al maestro tras una latencia fijada (T_w) enviando otro pulso.

3. El maestro detecta la respuesta del esclavo y mide el RTT ($\hat{T}_{RTT}$) para estimar la distancia.

El proceso descrito anteriormente se utiliza tanto con detección de amplitud como con detección de energía; únicamente la técnica de detección de los pulsos cambia. Podría pasar que el maestro no detecta ningún pulso en una trama, por lo que no sería posible realizar la estimación en dicha trama. La probabilidad de detección se define como la probabilidad de que la anterior situación no se produzca. Si denotamos tal probabilidad de detección con P_D^T, entonces la tasa efectiva de actualización de la medida sería $R_f^{eff} = P_D^T R_f$.

Idealmente, el RTT estimado sería $\hat{T}_{RTT} = 2T_p + T_w$, donde T_p es el tiempo de propagación del pulso, que se relaciona con la distancia como $T_p = \frac{c}{d}$, siendo d la distancia y c la velocidad de la luz. Por lo tanto, la distancia es estimada a partir del RTT como

$$\hat{d} = c\frac{\hat{T}_{RTT} - T_w}{2} \tag{3.1}$$

La expresión anterior es válida si la medida es no sesgada, es decir, si la media del error es nula. En caso contrario se debería realizar un proceso de calibración, tal y como se describe en [1].

El proceso de medición mediante el RTT se ilustra gráficamente en la Figura 3.3. Cabe destacar que la tasa de actualización de la medida está directamente relacionada con la máxima distancia que puede ser medida, tal y como se muestra en las siguientes expresiones

$$\begin{array}{c} T_{RTT}^{max} = T_f - T_b \\ T_p^{max} = \frac{T_{RTT}^{max} - T_w}{2} \\ d^{max} = c \cdot T_p^{max} \end{array} \tag{3.2}$$

Para una descripción más detallada, véase esta misma sección en el documento original (Apéndice A).

3.3. Análisis Teórico

Esta sección presenta un análisis teórico más elaborado del proceso de medida del tiempo de ida y vuelta de los pulsos UWB. Se analiza primero el proceso de medida del RTT de forma genérica, para luego detallar el análisis para cada una de las dos técnicas de detección estudiadas. Se analizan factores como la probabilidad de detección y la distribución estadística del error de estimación del RTT. Dicho análisis junto con las correspondientes expresiones matemáticas no se muestran en esta versión de la memoria, pero pueden encontrarse en esta misma sección del documento original (Apéndice A).

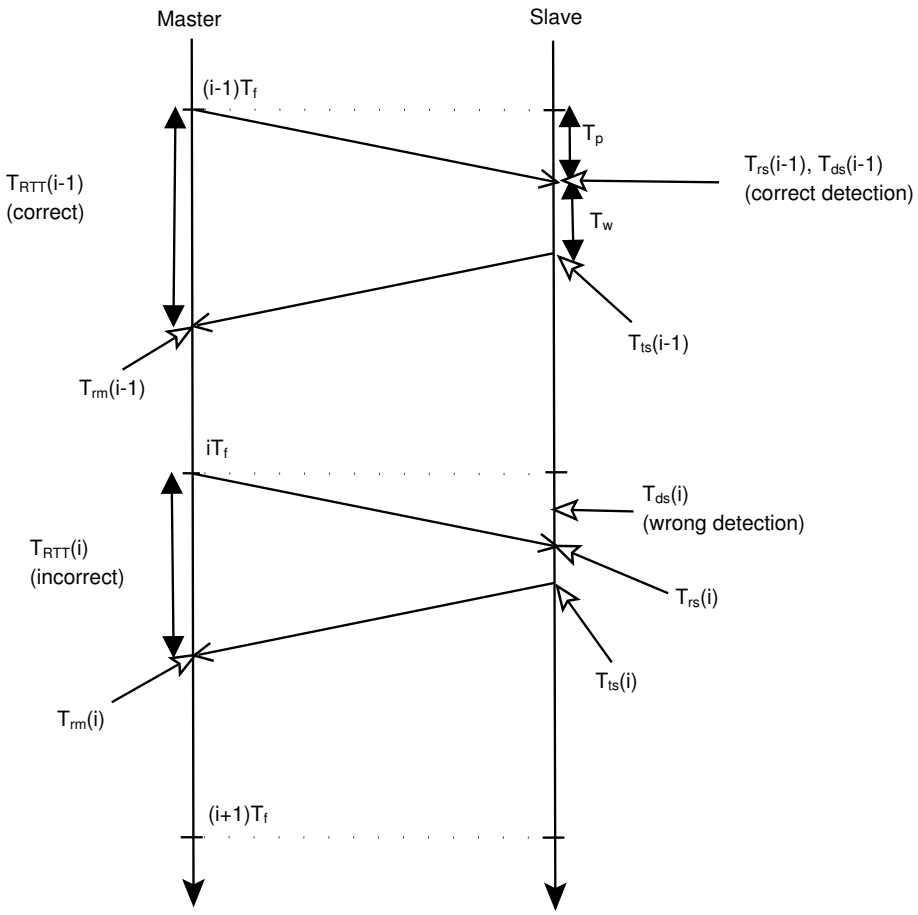

Figure 3.3: Diagrama temporal del proceso de estimación del RTT. Se muestran dos mediciones (tramas). En la trama (i-1) el pulso es detectado correctamente en el esclavo. Por otro lado, en la trama i el esclavo detecta el pulso cuando todavía no está presente, debido al efecto del ruido, y por lo tanto la estimación del RTT es errónea.

3.4. Selección del Umbral

Dado que esta sección esta muy relacionada con la anterior, se recomienda consultar este capítulo en la versión original del Apéndice A para entender mejor las expresiones que se muestran a continuación.

Existen dos opciones para calcular el umbral de detección. Una es fijar la probabilidad de detección que se desea para una cierta SNR, para lo cual se usan las aproximaciones teóricas de la probabilidad de detección que se muestran en la versión original del Apéndice A. Sería aconsejable establecer un margen de protección, es decir, si se espera tener un cierto valor de SNR, calcular el umbral con una SNR menor.

La otra alternativa, es fijar una cierta probabilidad de falsa alarma "instantánea"[1], la cual se denota por p_d. En este caso sólo es necesario conocer la potencia de ruido. Las expresiones para esta alternativa se muestran a continuación para detección de amplitud y detección de energía.

Detección de amplitud

$$\gamma_A = \sigma Q^{-1}\left(p_d^A\right) \tag{3.3}$$

donde $Q^{-1}(\cdot)$ es la función inversa del complemento de la función de distribución de la normal estándar. La potencia de ruido es σ^2.

Detección de energía

$$\gamma_E = \frac{\mathcal{N}_0}{2} Q^{-1}_{\chi^2_{2T_I B}}\left(p_d^E\right) \tag{3.4}$$

siendo $Q^{-1}_{\chi^2_\nu}(\cdot)$ la función inversa del complemento de la función de distribución de una distribución chi-cuadrado con ν grados de libertad. $\mathcal{N}_0$ representa la distribución espectral de potencia del ruido.

[1] Ya que el sistema es analógico, se habla de probabilidad de falsa alarma "instantánea", es decir, la probabilidad de que la señal de ruido (sin presencia de pulso) supere el umbral en un instante de tiempo.

Capítulo 4

Diseño Frontal de receptores UWB no coherentes

Este capítulo describe el diseño frontal de los receptores no coherentes realizados durante este PFC. La arquitectura del sensor está basada en el diseño previo descrito en [1]. En este PFC, el diseño se ha centrado la parte del receptor. Dos diseños diferentes se han llevado a cabo, uno para detección de amplitud y otro para detección de energía, implementándose dos placas de cada diseño, ya que tanto el maestro como el esclavo utilizan el mismo diseño. El diseño de las placas se ha realizado utilizando el software Eagle.

4.1. Arquitectura del sensor

La arquitectura del sensor se muestra en la Figura 4.1. Se compone de una sección analógica UWB de medida y una sección de procesamiento digital, basada en una FPGA. Conceptualmente, el interfaz entre la sección analógica UWB y la sección de procesamiento digital es proporcionada por medio de un conversor tiempo-digital (TDC), que proporciona medidas del RTT con una resolución de 65 ps. Además, un conversor digital-analógico (DAC) de 12 bits es usado para fijar el umbral para la detección en la sección del receptor UWB. Dicho DAC es programado por la FPGA.

Lo único que cambia en los dos diseños (detección de amplitud y detección de energía) es el transceptor UWB. Dicho transceptor se ilustra en el diagrama de bloques de la Figura 4.2. En el caso de detección de amplitud se utiliza simplemente un comparador (véase la Figura 3.1), mientras que en el caso de detección de energía se utiliza un detector de energía (ED), el cual incluye un dispositivo cuadrático, un integrador y un comparador (véase la Figura 3.2). Además el diseño incluye dos amplificadores de bajo ruido (LNA) que no se incluye en la Figura 4.2.

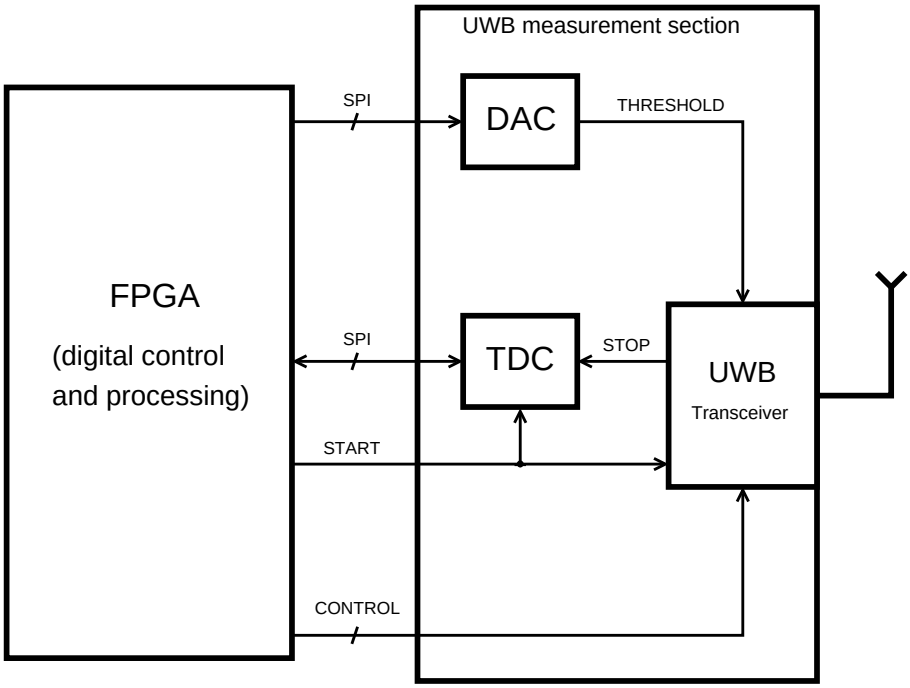

Figura 4.1: Diagrama simplificado de la arquitectura del sensor UWB. La sección analógica UWB se conecta a la FPGA mediante conexiones de interfaz de periférico serie (SPI) al TDC y al DAC para su configuración. La conexión entre el TDC y la FPGA también se usa para leer las mediciones de RTT. La FPGA controla el transceptor directamente con señales digitales de control.

La sección de procesamiento digital permite controlar los parámetros temporales y operacionales del sensor. En particular, tal y como se muestra en la Figura 4.1, la sección de medición requiere varias señales digitales de control. Las funciones de la sección digital se enumeran a continuación:

- **Controlar el transmisor UWB**: La medición se inicia cuando el maestro pregunta al esclavo mediante la transmisión de un pulso UWB. La señal de disparo del transmisor se genera digitalmente. Es posible ajustar dinámicamente la duración de trama, T_f (tasa de actualización de la medida).
- **Configurar y controlar el TDC**: El TDC se configura para realizar la medición. La medida en el TDC se inicia cuando el pulso es transmitido. El TDC se comunica a través de un interfaz SPI.
- **Controlar el switch**: El switch que selecciona la transmisión o recepción se controla digitalmente.

Tabla 4.1: Lista de Componentes

Componente	Referencia y proveedor
TDC	TDC-GP2, Acam Messelectronic
DAC	ADC5620, Analog Devices
Diodo generador de pulsos	5082-0112, HP
Switch	RSW-2-25P, Mini Circuits
LNA	MBC13720, Freescale Semiconductor
Comparador	LT1720, Linear Technology
Detector de energía (ED)	LTC5536, Linear Technology

- **Configurar el DAC** para el umbral de detección: El valor del umbral para detectar el pulso a la salida del comparador/ED es fijado digitalmente. Se puede fijar a priori o se puede calcular adaptativamente dependiendo de la probabilidad de falsa alarma requerida.
- **Estimación de la distancia**: Una vez que el maestro recibe la respuesta del esclavo, se calcula la distancia a partir de la lectura del RTT del TDC.

La FPGA proporciona flexibilidad en el desarrollo, implementación y ajustes de los algoritmos. El modelo de FPGA usado es el ML505 Virtex-5. La FPGA proporciona un control reconfigurable del sensor UWB.

4.2. Hardware: Selección de los componentes

La sección UWB de medición se ha implementado con una placa de circuito impreso en sustrato FR4 con una grosor de 1.0 mm. En este PFC, el esfuerzo en el diseño de los sensores se ha centrado en la parte del receptor, especialmente en la selección del LNA, comparador y ED.

En un principio se realizó una búsqueda de componentes adecuados para este diseño y fueron priorizados teniendo en cuenta distintas características en función de las necesidades. Por ejemplo, en el caso del LNA, se tuvo en cuenta el ancho de banda de operación, la figura de ruido, la ganancia y el consumo de corriente. Una descripción detallada del proceso de selección de los componentes se encuentra en la correspondiente sección de la versión original (apéndice A).

La Tabla 4.1 muestra los componentes que han sido utilizados en el diseño final de los sensores UWB.

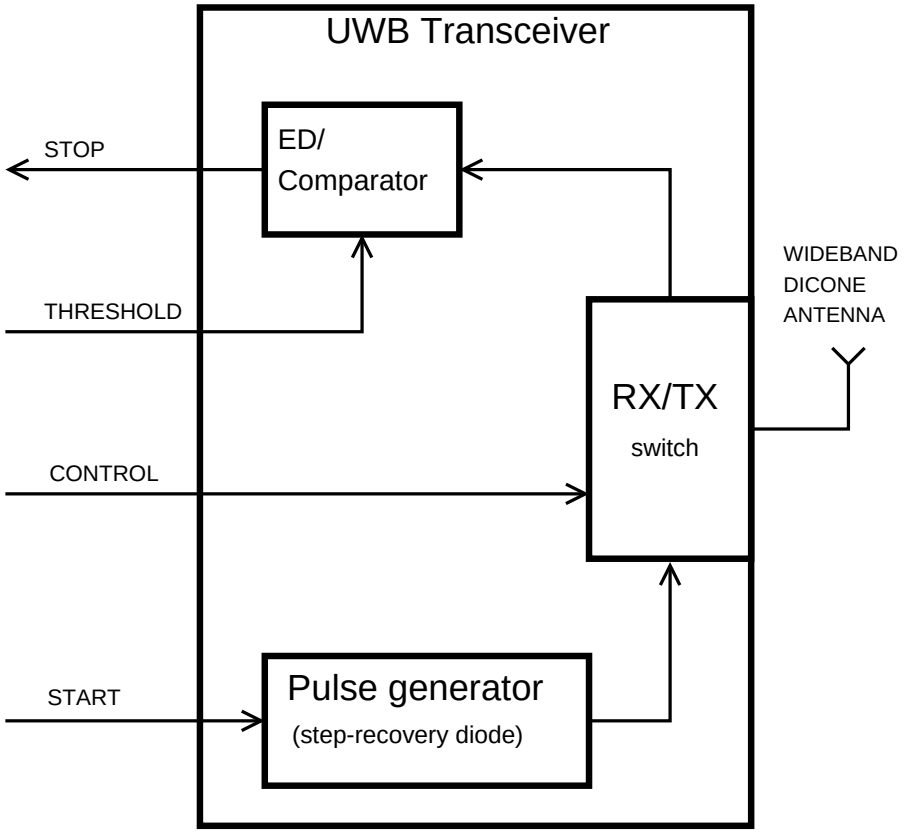

Figura 4.2: Arquitectura del transceptor UWB. El generador de pulsos está realizado usando un diodo de recuperación escalonada basado en el circuito caracterizado en [16] y se controla mediante la señal "start" de la FPGA. La salida del detector de energía/comparador proporciona la señal "stop" que controla la medición del TDC. El switch selecciona la posición RX o TX mediante una señal digital proporcionada por la FPGA. Para la transmisión y recepción de los pulsos UWB se utiliza una antena discono omnidireccional de banda ancha.

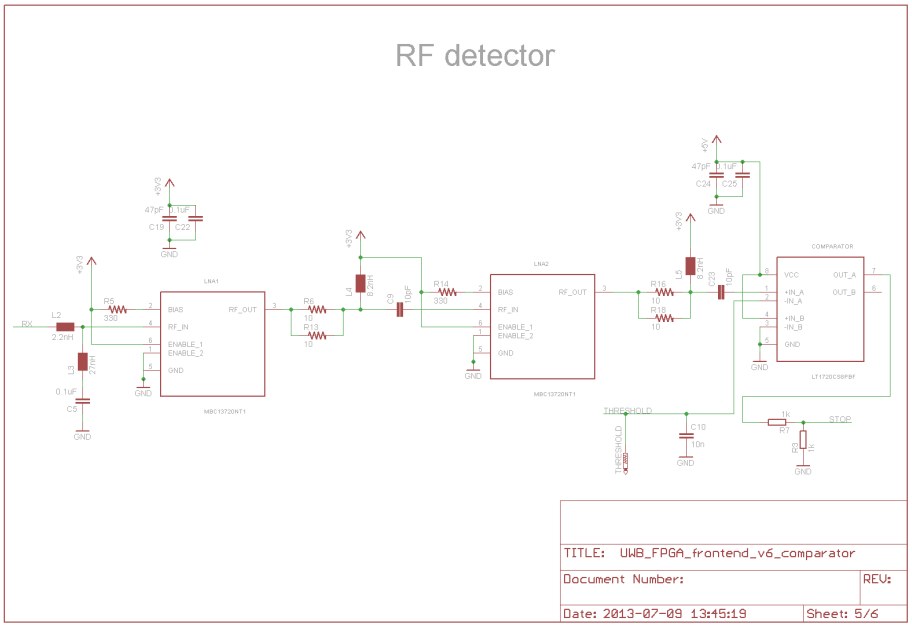

Figura 4.3: Esquemático del receptor no coherente utilizando detección de amplitud.

4.3. Implementación

En el diseño final, se conectaron dos amplificadores LNA en cascada, para así incrementar la sensibilidad del detector. Los esquemáticos de los transceptores a partir de los cuales se realizaron los circuitos impresos se muestran en las Figuras 4.3 (detección de amplitud) y 4.4 (detección de energía). El esquemático para detección de amplitud es igual al de detección de energía, pero reemplazando el ED por un comparador.

Además en las Figuras 4.5 (detección de amplitud) y 4.6 (detección de energía) se muestran fotografías de placas implementadas.

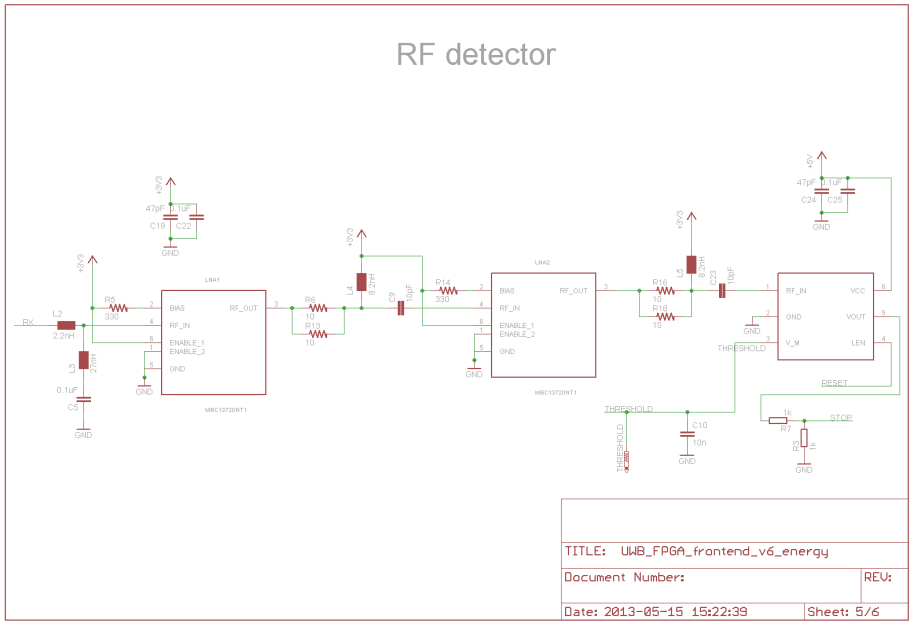

Figura 4.4: Esquemático del receptor no coherente utilizando detección de energía.

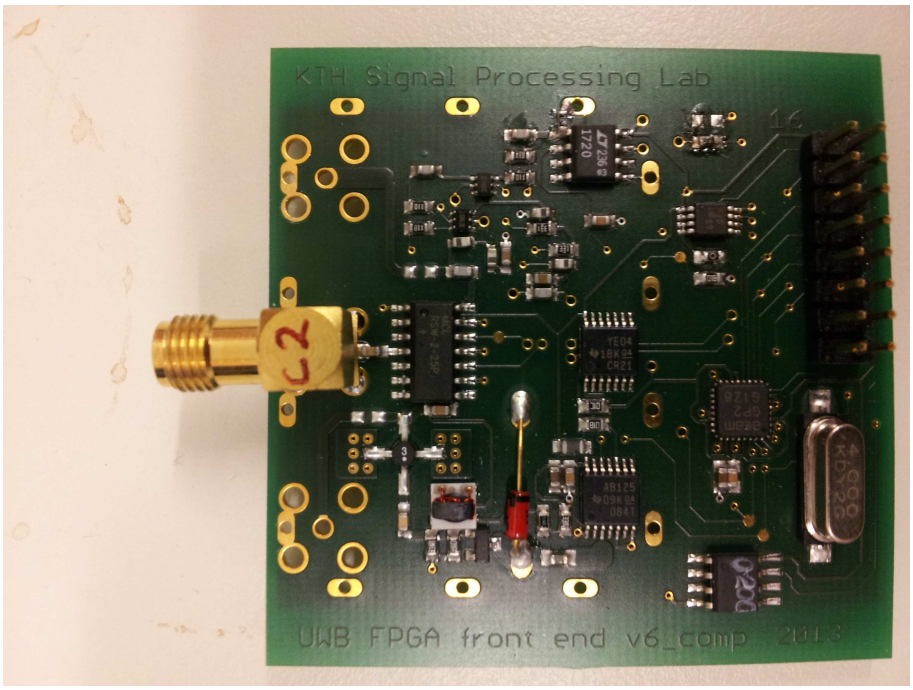

Figura 4.5: Fotografía de la placa implementada para detección de amplitud

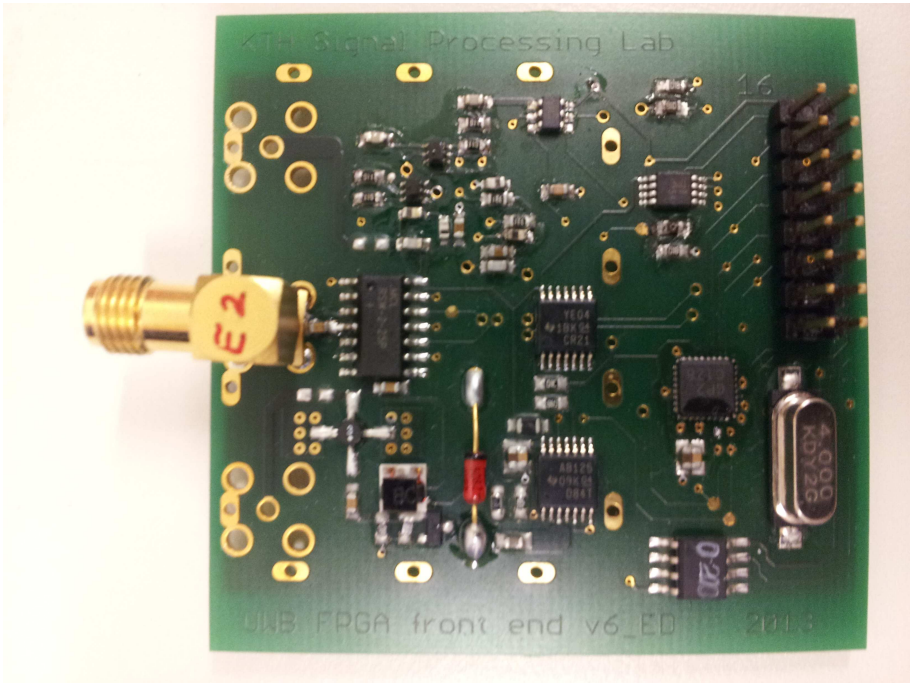

Figura 4.6: Fotografiía de la placa implementada para detección de amplitud.

Capítulo 5

Resultados de las Simulaciones

Este capítulo presenta los resultados de las simulaciones que se han llevado a cabo en este PFC. Las simulaciones se han realizado en MATLAB. En esta versión se muestran los resultados más importantes, pero se recomienda leer la versión completa de este capítulo en el apéndice A.

Principalmente, para el análisis del rendimiento, se utilizan la varianza del error en la estimación del RTT y probabilidad de detección. La precisión de la medida está relacionada con la varianza, es decir, cuanto menor es la varianza, mejor es la precisión. La varianza y la probabilidad de detección se calculan estadísticamente a partir de la repetición de del proceso de medida un número suficientemente alto de veces.

En las gráficas se muestra la varianza del error del RTT y en ningún momento se habla realmente de distancias, pero la conversión a varianza de distancia puede ser fácilmente realizada: $\sigma_d^2 = c^2\sigma_{\xi_t}^2$, siendo c la velocidad de la luz.

Los parámetros que componen un escenario de simulación se detallan a continuación:

- Receptor o detector (ideal, detección de amplitud, detección de energía)
- Forma de onda del pulso UWB (véase sección 2.1)
- SNR, definida como $\frac{E_b}{\mathcal{N}_0}$.
- Umbral (γ_A y γ_E para detección de amplitud y detección de energía, respectivamente). Véase la sección 3.4 para conocer cómo se calculan dichos umbrales.
- Tiempo de propagación del pulso, T_p, relacionado con la distancia: $d = cT_p$

- Latencia del esclavo, T_w: Es el tiempo que tarda en responder el esclavo desde que detecta la llegada de un pulso.
- Duración de trama, T_f. Es el periodo de repetición con el que el maestro transmite los pulsos y el inverso de la tasa de actualización de la medida (R_f). Fija el máximo tiempo de propagación del pulso que se puede medir correctamente: $T_p^{max} = \frac{T_f - T_w}{2}$
- Tiempo de la ventana de integración, T_I (sólo para detección de energía).

Ya que hay un número elevado de figuras para mostrar los resultados, y éstas se incluyen en la versión original con su correspondiente explicación; para evitar la excesiva duplicación de dichas figuras, no se incluyen en esta síntesis de la versión original. Por ello, véanse las secciones 5.1 y 5.2 de la versión original en el Apéndice A.

A continuación, se resumen los principales resultados correspondientes a las simulaciones del proceso de medida de RTTs utilizando receptores UWB no coherentes.

Probabilidad de detección

En cuanto a probabilidad de detección, el rendimiento podría medirse como la SNR necesaria para alcanzar una cierta probabilidad de detección con un cierto umbral.

En cuanto a las distintas formas de pulso, se observa que sólo existen diferencias entre ellas en cuanto al rendimiento en la detección de amplitud; debido a que los distintos pulsos tienen distinta amplitud para la misma energía (véase Tabla 2.1). Esto no ocurre con la detección de energía. De esta forma, usando detección de amplitud, el pulso que presenta mejores prestaciones es el monociclo de Scholtz; mientras que para detección de energía es indiferente.

Entonces, si comparamos ambas técnicas de detección (usando el monociclo de Scholtz) se observa que si se calcula el umbral con la misma probabilidad de falsa alarma instantánea (véase sección 3.4), la detección de amplitud requiere menor SNR para alcanzar la misma probabilidad de detección.

Precisión

La precisión de la medida está ligada a la probabilidad de falsa alarma "instantánea" (p_d), ya que los errores considerables se producen por falsas alarmas, es decir, cuando se produce una detección en ausencia del pulso. Por este motivo, un umbral dado fija una precisión que no puede mejorarse ni siquiera aumentando infinitamente la SNR. Tal precisión se alcanza cuando la probabilidad de

detección es cercana a 1. De esta forma, se puede decir que hay un compromiso entre probabilidad de detección y precisión; ya que para un cierto valor de SNR, la precisión mejora conforme se aumenta el umbral, pero a su vez si se aumenta demasiado el umbral, la probabilidad de detección puede disminuir, afectando también a la precisión.

Comparando la detección de energía con la de amplitud, se observa que con el mismo p_d (probabilidad de falsa alarma "instantánea") la precisión que se consigue es mejor con detección de energía. Sin embargo, se requiere más SNR para alcanzar dicha precisión.

Influencia del tiempo de propagación (distancia) y de la latencia del esclavo

Tanto el tiempo de propagación del pulso como la latencia del esclavo, especialmente ésta última ya que suele ser mayor, también influyen en el funcionamiento del proceso de medición. Lo que sucede es que el tiempo que transcurre entre el inicio de la medición y la llegada del pulso, está relacionado con la probabilidad de que se produzca una falsa alarma[1]. Es decir, si se mantiene el umbral (probabilidad de falsa alarma instantánea), pero se aumenta la latencia del esclavo, será más probable el hecho de que se produzca una falsa alarma, produciendo una varianza del error mayor.

Se puede apreciar en los resultados de las simulaciones que este hecho afecta en mayor medida a la detección de amplitud que a la detección de energía.

Influencia del tiempo de la ventana de integración

Básicamente, se observa que en el caso de detección de energía, la precisión mejora aumentando el tiempo de la ventana de integración.

[1] No confundir con la probabilidad de falsa alarma instantánea.

Capítulo 6

Estimación de distancia con UWB y submuestreo

Este capítulo presenta el método propuesto que permite reconstruir un pulso UWB a partir de un tren de pulsos utilizando submuestreo. El objetivo es intentar aproximar el rendimiento del receptor ideal, sin la complejidad impuesta por la alta tasa de muestreo necesaria.

6.1. Principio de funcionamiento

Este método probablemente sea más adecuado para medir tiempos de llegada (TOA) que para tiempos de ida y vuelta (RTT), ya que el submuestreo sólo puede ser utilizado en uno de los sensores. De forma que para medir RTTs, en el esclavo habría que utilizar detección no coherente. De esta manera, se mejoraría la precisión del receptor no coherente, pero no se podría lograr el mismo rendimiento que con el receptor ideal. Si fuese posible la sincronización de los sensores, podrían medirse TOAs, evitando la necesidad de utilizar detección no coherente. A continuación se describe el funcionamiento utilizando medidas de RTTs.

La señal recibida por el maestro sería un tren de pulsos

$$r_m(t) = \sum_{i=0}^{N_p-1} \sqrt{E_b} p(t - iT_d - T_{RTT}) + n(t) \tag{6.1}$$

siendo T_d el retraso entre pulsos consecutivos y N_p el número total de pulsos transmitidos por el esclavo. El retraso entre pulsos se fija como

$$T_d = t_s - T_b/N_s \tag{6.2}$$

donde t_s es el tiempo entre muestras y N_s es el número de muestras que se requieren en el pulso reconstruido, es decir, la resolución del pulso sería $\frac{T_b}{N_s}$,

siendo T_b la duración del pulso. Dicha resolución es precisamente la diferencia que existe entre el tiempo de muestreo y el retraso entre pulsos, lo que permite la reconstrucción del pulso submuestreando el tren de pulsos. Para asegurar la reconstrucción del pulso, el número de pulsos transmitidos debe ser

$$N_p = \frac{(T_{RTT}^{max} + T_b)\, N_s}{T_b} + 1 \tag{6.3}$$

siendo T_{RTT}^{max} el máximo RTT que se desea medir. En la Figura 6.1 se muestra un ejemplo sencillo de cómo se reconstruye el pulso a partir del tren de pulsos mediante el submuestreo. La Figura 6.2 muestra en un diagrama temporal el proceso de transmisión de los pulsos. Hay un compromiso entre el rango de medición ($T_{RTT}^{max} = t_s - T_b$) y la tasa de actualización de la medida, siendo la duración de una medición (trama)

$$T_f = t_s \cdot N_p \tag{6.4}$$

Así, que para mantener el mismo rango de medida que en el receptor ideal (o no coherente), la tasa de actualización de la medida se debe reducir. El consumo de potencia para transmitir todos los pulsos es $\frac{(N_p+1)E_b}{T_f}$, bastante mayor que con el detector no coherente con la misma tasa de actualización.

Básicamente, la señal recibida muestreada es la forma de pulso original, con un retraso que depende precisamente del RTT. Dicha señal recibida puede expresarse como

$$r_m\,[n] = \sqrt{E_b} p\left(n\frac{T_b}{N_s} - n_k\right) + v\,[n]\,;\, n = 0 \ldots N_p - 1 \tag{6.5}$$

El retraso, n_k, está relacionado con el RTT de la siguiente forma

$$n_k = \frac{T_{RTT} N_s}{T_b} \tag{6.6}$$

Una vez que el pulso es reconstruido, éste se detecta de la misma forma que en el detector ideal, es decir, calculando la correlación con una máscara del pulso original, obteniéndose así una estimación $\hat{n}_k$. El RTT se calcula sencillamente despejando de 6.6:

$$\hat{T}_{RTT} = \frac{\hat{n}_k T_b}{N_s} \tag{6.7}$$

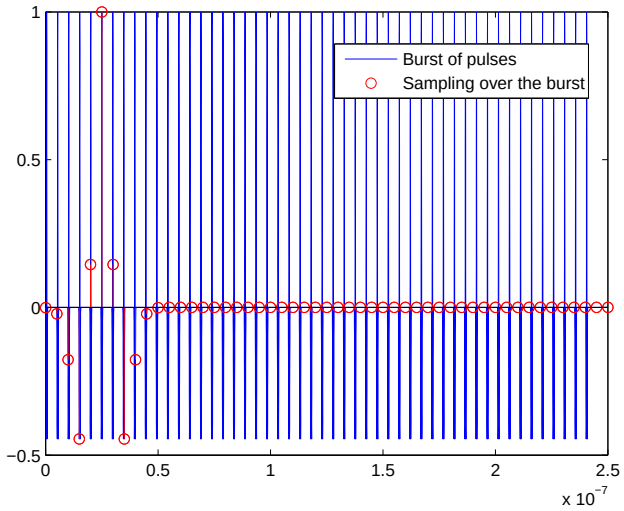

(a) $T_{RTT} = 0\,ns$

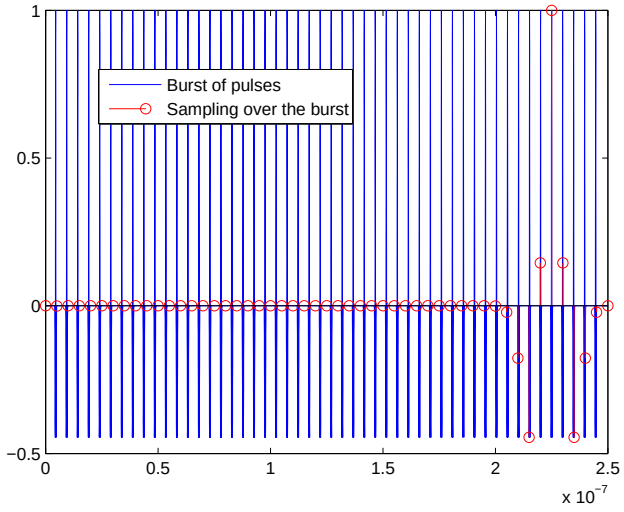

(b) $T_{RTT} = 4\,ns$

Figura 6.1: Ejemplo sencillo de cómo el submuestreo del tren de pulsos permite reconstruir el pulso original. El pulso usado es el monociclo de Scholtz. La duración de pulso, tasa de muestreo, y número de muestras del pulso reconstruido toman los siguientes valores: $T_b = 1\,ns$, $t_s = 5\,ns$, $N_s = 10$. (a) $T_{RTT} = 0\,ns$, (b) $T_{RTT} = 4\,ns$.

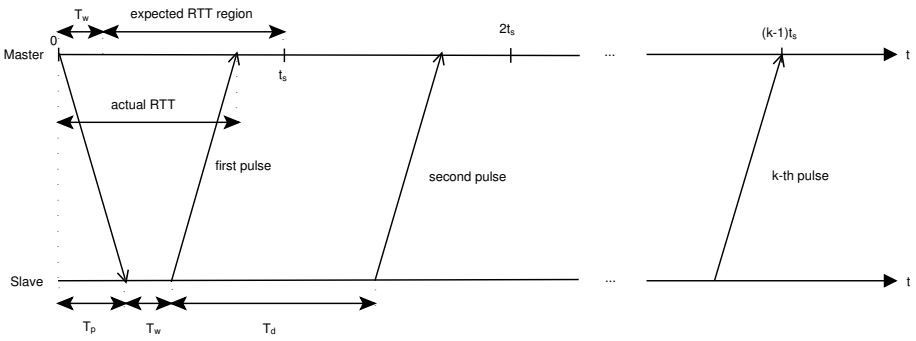

Figura 6.2: Diagrama temporal del proceso de medida del RTT usando submuestreo sobre un tren de pulsos.

Capítulo 7

Conclusiones

A continuación se resumen brevemente en una lista las conclusiones que se extraen de este PFC.

- Los receptores UWB no cohrentes parecen ser adecuados para la medida de distancias basándose en tiempos de ida y vuelta. El rendimiento es peor que el del receptor ideal, pero la pérdida no es grande y se gana simplicidad.
- La detección de energía parece presentar mejor precisión, a costa de requerir mayor SNR para funcionar correctamente.
- La detección de amplitud puede ser útil en lugares donde no es posible conseguir una SNR alta. Sin embargo, para distancias y/o latencias del esclavo largar, la precisión puede empeorar considerablemente.
- Es deseable que la latencia del esclavo sea lo más corta posible para así reducir la tasa de falsa alarma y por lo tanto, mejorar la precisión; especialmente para detección de amplitud ya que la precisión se ve más afectada que para detección de energía.
- El receptor propuesto que se basa en el submuestreo podría mejorar el rendimiento de los receptores no coherentes, a costa de mayor complejidad del diseño. La tasa de muestreo debe ser muy precisa. En estos momentos, parece difícil implementar este método, pero podría ser usado como punto de partida en futuras investigaciones.

7.1. Discusión

7.1.1. Detección de amplitud

El receptor UWB no coherente usando detección de amplitud es muy simple, sólo se necesita comparar la amplitud de la señal recibida con un umbral tras el

filtrado y la amplificación. La principal ventaja es la baja SNR que se necesita para alcanzar altas probabilidades de detección. Por otro lado, los RTTs largos empeoran considerablemente la precisión debido a las falsas alarmas. Por lo tanto, para bajas SNR y si la latencia del esclavo no es demasiado larga, puede ser una buena opción.

7.1.2. Detección de energía

El receptor no coherente usando detección de energía es más robusto frente a falsas alarmar para RTTs largos. Necesita de una mayor SNR para alcanzar alta probabilidad de detección. La tasa de falsa alarma es menor debido a la integración que se realiza al calcular la energía, lo que es equivalente a que el ruido es promediado.

7.1.3. Formas de onda de pulsos UWB

La principal diferencia entre los distintos pulsos es el rendimiento de detección, principalmente para detección de amplitud. Para detección de energía la diferencia entre los distintos pulsos es despreciable, mientras que en detección de amplitud el monociclo de Scholtz presenta el mejor comportamiento, por lo que en cuanto a probabilidad de detección es la mejor opción.

7.1.4. Detección de amplitud vs detección de energía

El diseño de ambos receptores es muy similar, únicamente hay que intercambiar un componente. Por lo tanto, en cuanto complejidad de diseño, no hay ninguna ventaja en escoger uno u otro.

Para RTTs cortos, la detección de amplitud parece presentar una mejor precisión (si se escogiese el umbral óptimo) que la detección de energía. Sin embargo, dado que la precisión en el caso de detección de amplitud se ve afectada en mayor medida conforme los tiempos de ida y vuelta aumentan, la detección de energía ofrecería una mejor precisión para RTTs más largos. Ya que en la práctica la latencia del esclavo suele ser muy larga comparada con el tiempo de propagación del pulso, la detección de energía es la mejor opción en general. La detección de amplitud podría ser más robusta en entornos hostiles donde la SNR suele empeorar, ya que la curva de detección es más suave con la detección de amplitud.

7.1.5. Diseño de los receptores

El diseño que se proporciona en este PFC es flexible y de baja complejidad. Ambas técnicas de detección se han implementado. Debido a la falta de tiempo, no ha sido posible realizar experimentos con las placas implementadas para su comparación con las simulaciones.

7.1.6. Receptor UWB con submuestreo

El método propuesto para reconstruir un pulso a partir de una ráfaga de pulsos mediante submuestreo es una idea que podría ser usada en el futuro. En estos momentos, parece complicada su implementación ya que requiere alta precisión de la tasa de muestreo y retraso de los pulsos.

7.2. Trabajo futuro

Las simulaciones realizadas en este PFC son válidas y pueden ser útiles para extraer conclusiones. Sin embargo, probablemente no coincidiría con los resultados de las simulaciones. La razón es que la latencia del esclavo en la práctica es muy larga. En estas simulaciones dicha latencia se ha considerado cero o muy corta porque sino el tiempo de ejecución de las simulaciones se vería incrementado en gran medida. Una posible continuación de este trabajo sería realizar simulaciones similares, pero con valores más reales de la latencia del esclavo.

Además, como se ha mencionado antes, no ha sido posible llevar a cabo experimentos debido a la restricción del tiempo y a que los último tres meses he trabajado desde España. De esta forma, el siguiente paso sería realizar experimentos con las placas implementadas.

Otro posible trabajo podría ser el desarrollo de un algoritmo para el ajuste dinámico del umbral de detección. La probabilidad de detección deseada sería fijada, y mediante procesado de señal el umbral sería aumentado o reducido en función de la estimación de probabilidad de detección. De esta forma, se conseguiría un umbral óptimo.

El receptor propuesto que utiliza submuestreo, podría ser usado en futuro como un punto de partida. El método podría ser mejorado para permitir el uso del submuestreo en ambos sensores (maestro y esclavo). Se podría considerar el uso de retrasos variables de los pulsos.

La naturaleza dispersiva de los canales UWB, lo cual provoca multicamino [11], no se ha considerado en este PFC. Este es un tema que debería ser tratado en futuras investigaciones en el contexto de receptores UWB no coherentes.

Bibliografía

[1] A. De Angelis, S. Dwivedi and P. Händel, *"Characterization of a Flexible UWB Sensor for Indoor Localization".*

[2] H. Liu, H. Darabi, P. Banerjee, and J. Liu, "Survey of Wireless Indoor Positioning Techniques and Systems," *Systems, Man, and Cybernetics, Part C: Applications and Reviews, IEEE Transactions on*, vol. 37, no. 6, pp. 1067–1080, Nov. 2007.

[3] I. Skog, P. Händel, J. Nilsson, and J. Rantakokko, "Zero-velocity detection – an algorithm evaluation," *IEEE Transactions on Biomedical Engineering*, vol. 57, no. 11, pp. 2657–2666, Nov. 2010.

[4] D. Zachariah and M. Jansson, "Camera-aided inertial navigation using epipolar points," in *Position Location and Navigation Symposium* (PLANS), 2010 IEEE/ION, May 2010, pp. 303–309.

[5] J. Rantakokko, J. Rydell, P. Strömbäck, P. Händel, J. Callmer, D. Törnqvist, F. Gustafsson, M. Jobs, and M. Gruden, "Accurate and reliable soldier and first responder indoor positioning: multisensor systems and cooperative localization," *IEEE Wireless Communications*, vol. 18, no. 2, pp. 10–18, Apr. 2011.

[6] G. Santinelli, R. Giglietti, and A. Moschitta, "Self-calibrating indoor positioning system based on ZigBee R devices," in *IEEE Instrumentation and Measurement Technology Conference*, May 2009, pp. 1205–1210.

[7] D. Macii, F. Trenti, and P. Pivato, "A robust wireless proximity detection technique based on RSS and ToF measurements," in *IEEE International Workshop on Measurements and Networking Proceedings (M&N)*, Oct. 2011, pp. 31–36.

[8] S. Gezici and H. Poor, *"Position estimation via ultra-wide-band signals", Proceedings of the IEEE,* vol. 97, no. 2, pp. 386-403, 2009.

[9] C. De Dominicis, A. Flammini, S. Rinaldi, E. Sisinni, A. Cazzorla, A. Moschitta, and P. Carbone, "High-precision UWB-based timestamping," in *International IEEE Symposium on Precision Clock Synchronization for Measurement Control and Communication (ISPCS)*, Sept. 2011, pp. 50–55.

[10] A. De Angelis, J. Nilsson, I. Skog, P. Händel, and P. Carbone, "Indoor Positioning by Ultrawide Band Radio Aided Inertial Navigation," *Metrology and Measurement Systems*, vol. 17, no. 3, pp. 447–460, 2010.

[11] I. Guvenc and Z. Sahinoglu, "Threshold-Based TOA Estimation for Impulse Radio UWB Systems".

[12] I. Guvenc, Z. Sahinoglu, and P. V. Orlik, "TOA Estimation for IR-UWB Systems With Different Transceiver Types" in *IEEE Transactions on Microwave theory and techniques*, vol. 54, no. 4, April 2006.

[13] *Revision of part 15 of the commission's rules regarding ultra-wideband transmission systems*, Federal Communication Commission Std., 2002, Report and order, in FCC 02 48, Apr. 2002.

[14] *Electromagnetic compatibility and Radio spectrum Matters (ERM); Ultra WideBand (UWB) technologies for communication purposes;* ETSI EN 302 065, ETSI Std., Rev. V1.1.1, February 2008.

[15] X. Chen and S. Kiaei, *"Monocycle Shapes for Ultra Wideband System".*

[16] A. De Angelis, m. Dionigi, R. Giglietti and P. Carbone, "Experimental comparison of low-cost sub-nanosecond pulse generators," *IEEE Transactions on Instrumentation and Measurement*, vol. 60, no 1, pp. 310-318, Jan. 2011

Apéndice A

Documento Original del Proyecto Fin de Carrera

KTH Electrical Engineering

Investigation of Variety of Non-Coherent Front end Detectors For Timing Estimation

LUIS LACASA CALVO

Stockholm 2013

Signal Processing
School of Electrical Engineering
Kungliga Tekniska Högskolan

XR-EE-SB 2013:007

Abstract

The indoor localization of mobile users is currently a central issue for many applications and fields, including sensor networks, asset management, healthcare, ambient-assisted living, and public safety personnel localization. Existing solutions often rely on the fusion of information from multiple sensors.

The potential of using an ultra wideband (UWB) system for wireless distance measurement based on the round-trip time (RTT) has been investigated in this thesis. Non-coherent UWB receivers have been analyzed using two different approaches: amplitude detection and energy detection. Both non-coherent UWB receivers front ends have been designed and implemented. Simulations of the measurement performance are also provided. Furthermore, a method has been proposed using undersampling over a burst of UWB pulses to reconstruct the original pulse and try to approximate the optimal performance of the ideal UWB receiver.

The simulations yield interesting results regarding the performance of the RTT estimation. Both detection techniques are compared, describing the advantages and disadvantages of each one.

Acknowledgements

I would like to thank to my supervisor of the thesis, Satyam Dwivedi, for giving me the opportunity to perform my master thesis in the department of Signal Processing, in the School of Electrical Engineering of the Royal Institute of Technology in Stockholm, and for his excellent guidance and advice during all the period I have worked in this project. I also want to thank to him his flexibility and availability, allowing me to work on my own, even in being in Spain during last months.

I also want to express my biggest thanks to my mother for giving me all the necessary support to perform this master thesis in Sweden, although this entailed several diculties.

Table of Contents

List of Figures

List of Tables

Nomenclature

ADC	Analog-to-Digital Converter
AWGN	Additive White Gaussian Noise
CDF	Cummulative Distribution Function
DAC	Digital-to-Analog Converter
ED	Energy Detector
FPGA	Field Programmable Gate Array
LNA	Low-Noise Amplifier
NF	Noise Figure
PDF	Probability Density Function
PSD	Power Spectral Density
RTT	Round-Trip Time
SNR	Signal-to-Noise Ratio
SPI	Serial Peripherical Interface
TDC	Time-to-Digital Converter
TOA	Time Of Arrival
UWB	Ultra-Wide Band

Chapter 1

Introduction

In this thesis the operation of ultra wideband (UWB) ranging sensors for personnel indoor localization based on the measurement of the pulse round trip time (RTT) is investigated. Two non-coherent receiver types are analyzed in order to find out the strengths of each one. The difference between such receivers is the employed method to detect the UWB pulses: amplitude detection and energy detection. The ideal UWB receiver is also analyzed to compare it with the non-coherent receivers. The utilization of the results given in this thesis could in the future have a broader help in the implementation of UWB ranging sensors.

This report gives theoretical analysis as well as the results of the simulations carried out during this master thesis work. Such results yield interesting features of the non-coherent receivers performance. The aim of this thesis has been to find out which of such non-coherent receivers works better in which situation. Different UWB pulse shapes are also considered.

The designs of both non-coherent receiver front ends have also been carried out in this thesis work and there is a chapter dedicated to describe such designs. The designs are based on the previous work done in the Signal Processing Lab at KTH [1].

A new method to try to approximate the performance of the ideal receiver using undersampling is proposed in this master thesis in chapter 6. This method could be in the future a start point to reconstruct a UWB pulse by sampling a burst of pulses without needing to use the Nyquist-rate.

1.1 Background

The indoor localization of mobile users is currently a central issue for many applications and fields, including sensor networks, asset management, healthcare, ambient-assisted living, and public safety personnel localization [2]. Existing solutions often rely on the fusion of information from multiple sensors. In particular, some of the most widely used sensor types are inertial navigation systems [3], imaging systems such as cameras or infrared sensors [4], ultrasonic ranging sensors [5], and radio-based positioning technologies.

Measuring the position of users accurately and reliably is of particular relevance for first responder localization scenarios, where location awareness in global navigation satellite systems (GNSS-denied) environments is an important tool for efficiency and safety [6]. The main mission-specific requirements for various types of professional users can be found in [7]. In such scenarios, solutions are often based on cooperative and opportunistic techniques, because the system provided must be operational even in the absence of a preinstalled localization infrastructure.

To experimentally investigate radio-based indoor distance and position measurement, numerous methods have been proposed in the literature. Systems such as that described in [8] are implemented using off-the-shelf, short-range wireless communication systems. Furthermore, for applications in which coarse distance information may be considered sufficient and accurate positioning is not a strict requirement, proximity detectors may be used, such as the nearly omnidirectional, ZigBee-based proximity detection technique described in [9].

On the other hand, the accurate ranging prototype described in [10] is an example of a dedicated stand-alone solution. Finally, experimental proof-of-concept demonstrators such as that presented in [11] are used to validate the algorithms developed using external electronic instrumentation.

In this context, ultra wideband (UWB) systems are the object of considerable research interest due primarily to their high ranging resolution and low power operation [12]. Recently, the potential benefits for time synchronization of wireless nodes derived from the use of UWB technology have also been investigated. In particular, [13] proposed a new hybrid wireless node consisting of a traditional IEEE802.15.4 radio supported by a UWB transceiver for precise timestamping. From a regulatory viewpoint, a UWB system is defined in [14] as any intentional radiator having a fractional bandwidth greater than 20% or an absolute bandwidth greater than 500 MHz. Moreover, spectral masks defining the upper limits on emissions are provided by regulatory agencies; see, e.g., [14, 15]. Typically, a motivation of the use of a UWB ranging system in a multisensor localization system is to prevent the growth of the error inherent in inertial navigation systems, because the error in UWB ranging estimates is bounded [16].

1.2 Motivation

The primary aim of this thesis has been to find out which UWB receptor is better in each situation for the RTT measurement. Furthermore, it is important to know which facts affect the performance of the measurement process.

Moreover, the sensor is designed to track mobile users and thus is not only for static measurements. Therefore, a high measurement update rate is a fundamental requirement to achieve high dynamic range tracking. In this context, an update rate of 100 Hz is desirable for accurate high dynamic range tracking. The sensor developed is designed to support update rates even exceeding this value. Furthermore, the sensor is a valuable tool for implementing cooperative localization techniques; see, e.g., [17]. The development of such techniques currently represents an open research problem and a fundamental element of first responder localization in the absence of infrastructure.

In the future it is possible that the UWB sensor developers would use the results given in this thesis to select the most suitable combination of UWB receiver, pulse shape and the signal processing parameters (such parameters will be further described in chapter 3) to achieve a sensor as accurate as possible.

1.3 Problem statement

Several studies have analyze the time-of-arrival (TOA) estimation using impulse radio (IR) UWB systems and sampling, e.g. [18, 19], however, such methods require synchronization. Moreover, the extremely wide band of UWB pulses makes very complex the sampling using the Nyquist-rate. Thus, in this thesis the non-coherent UWB receivers are investigated. The RTT is used for the distance measurement instead of the TOA, thus no synchronization between sensors is needed.

The development of the sensor described in this thesis follows a novel approach combining several key aspects [1]:

- round-trip-time-based distance measurement,
- modularity and flexibility of the architecture,
- emphasis on the digital signal processing capabilities,
- asynchronous operation,
- high measurement update rate,
- design based on time-to-digital converter (TDC).

These features make the sensor particularly suitable for experimental research in first responder indoor localization applications, mainly because round-trip-time ranging does not rely on a preinstalled infrastructure and the TDC makes it possible to achieve high ranging accuracy with low complexity and low power.

1.3.1 UWB Non-Coherent Receiver Types

Two types of UWB non-coherent receivers are considered in this thesis. They will be further described in chapter 3.

1.3.1.1 Energy Detection

The energy detection (ED) approach is widely studied in the UWB literature. The UWB pulse is detected by comparing the energy of the received energy with a threshold. It is explained in section 3.3.2

1.3.1.2 Amplitude Detection

In this case the amplitude of the received signal is compared with a threshold in order to detect the UWB pulse. It will be further described in section 3.3.1. Amplitude detection is not so studied in the literature as ED, but although the performance is worse than ED, it can be suitable for some situations as it will be shown in the results in chapter 5.

Formulation of the Main Objective of this Thesis This thesis has tried to find out which aspects affect and how they affect to the performance of the distance measurement using non-coherent UWB receivers based on the round-trip-time in order to select the most suitable configuration (receiver type, pulse shape, etc) for some specific conditions.

1.4 Thesis organization

The second chapter will introduce the reader to the basics of the UWB signals and the ideal UWB receiver. Different UWB pulse shapes are described. Furthermore it gives a description of the ideal UWB receiver.

The third chapter of this report describes two types of non-coherent UWB receivers, amplitude and energy detection. It is dedicated to present the basics and theory related to the systems which have been investigated and simulated in this master thesis work. The RTT measurement process is described and analyzed.

Chapter four presents the design of the UWB non-coherent front ends which have been carried out in this thesis work, based on the previous work performed in the Signal Processing Lab at KTH. A list of the components used in such design is given. Pictures of the implemented boards are shown.

The fifth chapter is dedicated to the results of the simulations carried out in order to compare the performance of amplitude and energy detection approaches as well as of the different UWB pulse shapes. Interesting results are given that may be used in future works to help to select which UWB non-coherent receiver pulse shape use.

In chapter six the proposed UWB ranging method using undersampling is presented.

Finally a chapter concludes this report with a discussion and comments on possible future work. All references to earlier studies as well as other sources of information can be found in the end of this report.

Chapter 2

UWB Signal and Ideal Receiver

In this chapter the reader will get basics of the UWB systems. It is dedicated to those who have no or little knowledge about UWB systems. The UWB signals and the ideal UWB receiver are described. Section 2.1 presents the different UWB pulse shapes that can be used. Furthermore, in section 2.2 the ideal UWB receiver is described.

From a regulatory viewpoint, a UWB system is defined in [14] as any intentional radiator having a fractional bandwidth greater than 20% or an absolute bandwidth greater than 500 MHz. Moreover, spectral masks defining the upper limits on emissions are provided by regulatory agencies; see e.g., [14, 15] Typically, a motivation of the use of a UWB ranging system in a multisensor localization system is to prevent the growth of the error inherent in inertial navigation systems, because the error in UWB ranging estimates is bounded [16].

In this chapter the RTT measurement procedure is not described, it is left for the next chapter, where the non-coherent receivers are described.

2.1 UWB Pulse Shapes

This section presents the different pulse or monocycle shapes which have been considered in this thesis. Such shapes are described in [20]. In this thesis, only the waveforms are shown, but in [20] the PSDs are also shown. The bandwidth is actually different for each shape and some of them are low-pass but others are band-pass. However, for simplicity, the bandwidth is assumed to be $\frac{1}{T_b}$ (T_b is the pulse duration) and low-pass for all the shapes. All the shapes are shown in Figure 2.1. The last plot shows all the different shapes together with the same energy, i.e. they have different amplitudes since for the same amplitude, the different shapes have different energy. Table 2.1 shows the energy of each shape in terms of the amplitude, as well as the 3-dB bandwidth of each pulse shape.

Table 2.1: Energy each shape in terms of the amplitude and 3-dB bandwidth of each shape.

Shape	Energy for in terms of A	3-dB Bandwidth
Gaussian pulse	$2.5066 \cdot 10^{-10} \cdot A^2$	0 - 1 GHz
Gaussian monocycle	$3.0113 \cdot 10^{-10} \cdot A^2$	500 MHz - 1.5 GHz
Scholtz's monocycle	$1.5 \cdot 10^{-10} \cdot A^2$	1 GHz - 2.3 GHz
Manchester monocycle	$10^{-9} \cdot A^2$	300 MHz - 1.2 GHz
RZ-Manchester monocycle	$k \cdot 10^{-9} \cdot A^2$	500 MHz - 1.4 GHz
Sine monocycle	$5 \cdot 10^{-10} \cdot A^2$	400 MHz - 1.3 GHz
Rectangle monocycle	$10^{-9} \cdot A^2$	0 - 1 GHz

We could relate the energy with the amplitude by $E_b = k_s T_b A^2$, where k_s is a parameter which depends on the pulse shape and $0 \leq k_s \leq 1$. The shapes expressions which are described below, $w(t)$, generate pulses that are non-zero in the interval $0.5 \cdot T_b \leq t \leq 1.5 \cdot T_b$ and with unit amplitude, but the pulse expression used during the whole thesis, $p(t)$, is non-zero within the interval $0 \leq t \leq T_b$ and with unit energy, thus to be coherent $p(t)$ and $w(t)$ are related by

$$p(t) = \sqrt{\frac{1}{k_s T_b}} w(t + 0.5 \cdot T_b) \tag{2.1}$$

Thus, the mathematical expressions for each UWB pulse shape with unit amplitude are presented in the following subsections.

2.1.1 Gaussian pulse

The Gaussian pulse can be represented by

$$w(t) = e^{-[(t-T_b)/T_{au}]^2} \tag{2.2}$$

where T_b is the duration and T_{au} is the pulse shape parameter. The actual pulse width is controlled by the pulse shape parameter. $T_{au} = 0.2 \cdot T_b$ is a suitable value, because otherwise, either part of the energy will be out of the duration interval or the energy will be concentrated in the center (i.e. the actual duration will not be T_b).

2.1.2 Gaussian monocycle

The Gaussian monocycle is similar to the first derivative of the Gaussian pulse and is given by [26]

$$w(t) = \frac{2}{T_{au}} \cdot \sqrt{e} \cdot (t - T_b) \cdot e^{-2 \cdot [(t-T_b)/T_{au}]^2} \tag{2.3}$$

$T_{au} = 0.25 \cdot T_b$ is a suitable value due to the same reason described in 2.1.1.

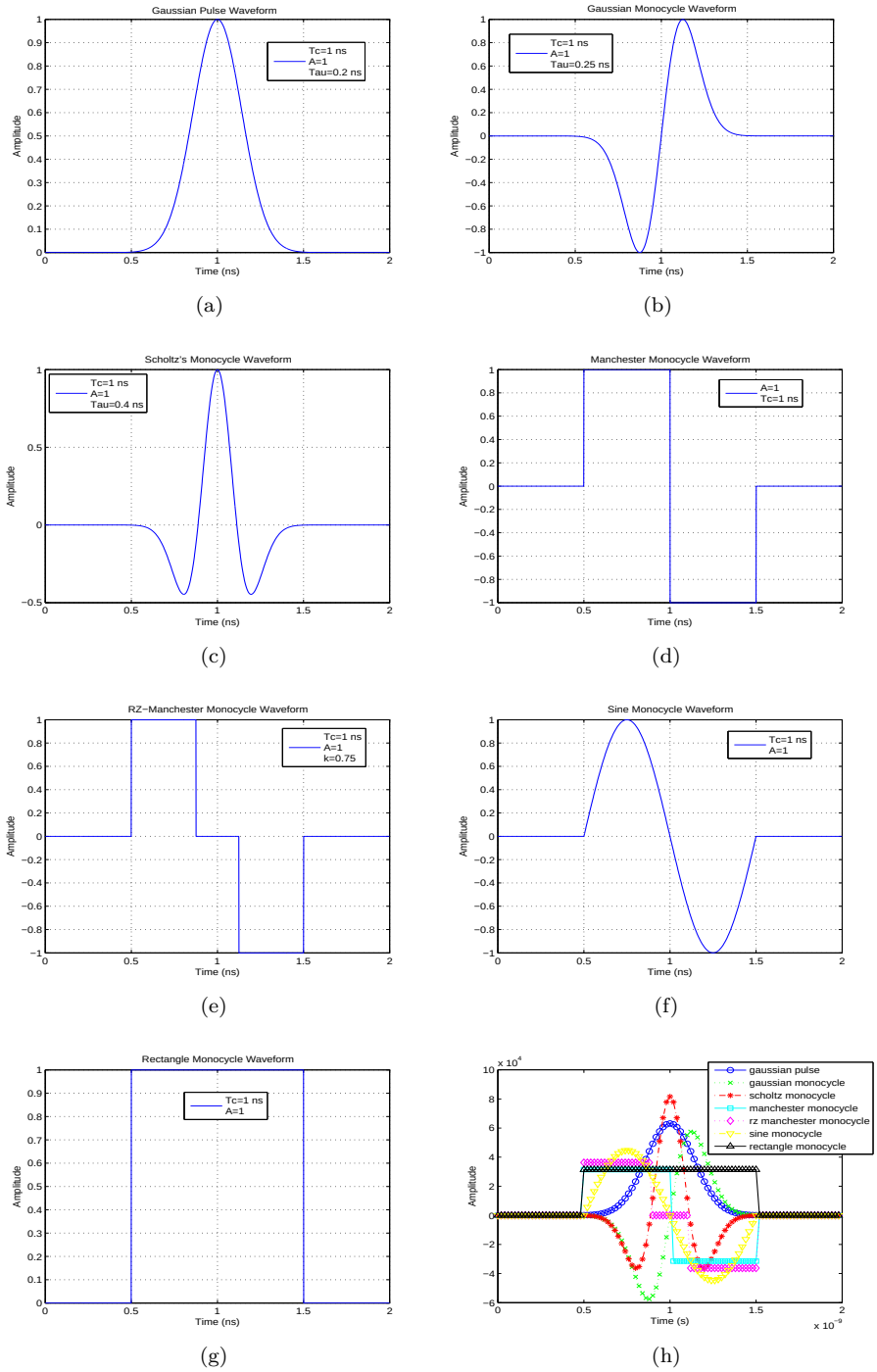

Figure 2.1: Shape Waveforms with duration $T_b = 1\,ns$: (a) Gaussian pulse, (b) Gaussian monocycle, (c) Scholtz's monocycle, (d) Manchester monocycle, (e) RZ-Manchester monocycle, (f) sine monocycle, (g) rectangle monocycle, and (h) all the shapes with the same energy in the same plot.

2.1.3 Scholtz's monocycle

Scholtz's monocycle is similar to the second derivative of the Gaussian and can be represented by [21]

$$w(t) = \left[1 - 4\pi\left(\frac{t - T_b}{T_{au}}\right)^2\right] e^{-2\pi\left(\frac{t-T_b}{T_{au}}\right)^2} \tag{2.4}$$

$T_{au} = 0.4 \cdot T_b$ is an adequate value in this case.

2.1.4 Manchester Monocycle

The Manchester monocycle has amplitude 1 during half of the monocycle width and has amplitude -1 during the other half

2.1.5 RZ-Manchester Monocycle

The return-to-zero Manchester monocycle (with unit amplitude) has amplitude 1 and -1 for only a portion of each half monocycle width. Such portion is represented by the parameter k ($0 < k \leq 1$).

2.1.6 Sine Monocycle

The sine monocycle is one period of a sine wave. The period of the sine wave is the pulse duration, T_b.

2.1.7 Rectangle Monocycle

The rectangle monocycle has uniform amplitude during the whole pulse width.

2.2 Ideal UWB Receiver

Although the objective of this thesis is not to investigate the ideal UWB receiver, it is interesting to analyze such receiver in order to compare the performance of the non-coherent UWB receivers and the proposed receiver using undersampling with such ideal receiver. This ideal receiver is based on the assumption that the UWB pulse can be sampled with a higher sampling frequency than the Nyquist rate. Due to the wide band of such pulses, the required sampling rate is very high, which makes the design to be very complex or even unfeasible.

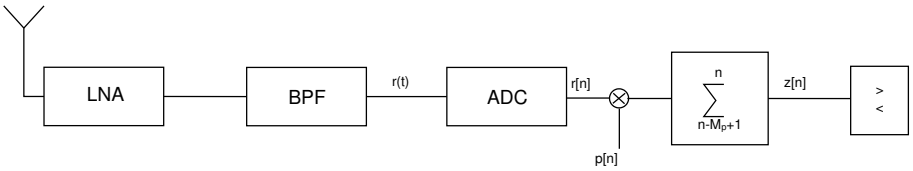

Figure 2.2: Block diagram of ideal UWB receiver

Thus, the ideal receiver is assumed to be able to over-sample the UWB pulse, thus allowing to correlate the received sampled signal with the known pulse shape. Let the UWB received signal after filtering and amplification be represented by

$$r(t) = \sqrt{E_b} p(t - t_d) + n(t) \tag{2.5}$$

where E_b is the received pulse energy after amplification and t_d is a generic delay of the pulse. Additive white Gaussian noise (AWGN) with zero-mean, double-sided power spectral density $\frac{\mathcal{N}_0}{2}$ and variance σ^2 is denoted by $n(t)$. Since the received signal is filtered, the bandwidth of the noise is limited. The variance or power of the noise is $\sigma^2 = \mathcal{N}_0 \cdot B$. The SNR is defined by $\frac{E_b}{\mathcal{N}_0}$.

After the filtering, the signal is sampled by an analog-to-digital converter (ADC) with sampling rate f_s, greater than the Nyquist rate, being the sampled signal

$$r[n] = r(nt_s) = \sqrt{E_b} p[n - n_d] + v[n] \tag{2.6}$$

where t_s is the inverse of the sampling rate (f_s), n_d is the delay in number of samples ($n_d = \frac{t_d}{t_s}$). The sampled noise is denoted by $v[n]$. Such signal is correlated with the known pulse shape and compare with a threshold in order to detect the pulse. The correlated signal can be expressed by

$$z[n] = \sum_{k=n-M_p+1}^{n} r[k] p[k - n + M_p - 1] \tag{2.7}$$

where $p[n]$ is the known pulse shape, which has M_p samples ($M_p = \frac{T_b}{t_s}$), being T_b the pulse duration. The block diagram of this ideal receiver is shown in Figure 2.2.

Thus, when $z[n]$ exceeds the threshold, γ, the receiver estimates that the pulse is present. Without considering the noise, the maximum of $z[n]$ would be $\sqrt{E_b}$ at index $n = round(n_d)$. Therefore, the threshold may be set as a percentage of $\sqrt{E_b}$

$$\gamma = k\sqrt{E_b}; 0 \leq k \leq 1 \tag{2.8}$$

Chapter 3

UWB Non-Coherent Receivers

Since the use of the ideal UWB receiver (described in section 2.2) is unfeasible and very complex, we are interested in designing a simpler receiver. Two non-coherent detection approaches are investigated: amplitude detection and energy detection. Such techniques are implemented in the analog domain, so it is not needed to sample the UWB signal, making the design much simpler.

The non-coherent receivers do not require channel estimation and have low-complexity implementation at the expense of performance loss. The suboptimal non-coherent receivers are suitable for low power and low-cost scenarios. The non-coherent receivers do not require synchronization, therefore it enables infrastructure-free and anchor-less localization. The detection is simply carried out by comparing some feature of the received UWB signal (amplitude or energy in the case of this thesis) with a threshold in a fully analog implementation.

3.1 Non-coherent receiver architecture

Two UWB non-coherent receivers are studied in this thesis. They are quite similar, only the technique to detect the UWB pulses changes. Both non-coherent receivers detect the pulses by comparing a feature of the received signal with a threshold. In both receivers the received signal is filtered and amplified. After that it is different in each one:

- **Amplitude detection approach**: The actual amplitude of the received signal after filtering and amplification is compared with a threshold, i.e. it only needs a comparator.
- **Energy detection approach**: In this case the received signal after filtering and amplification is passed through a square-law device and an integrator with integration time T_I before comparing with the threshold.

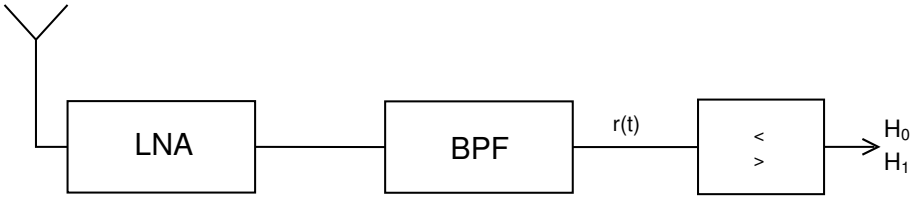

Figure 3.1: Simplified block diagram of non-coherent UWB receiver using amplitude detection approach.

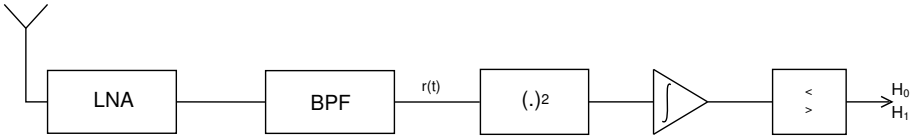

Figure 3.2: Simplified block diagram of non-coherent UWB receiver using energy detection approach.

> Therefore, the energy of the signal within intervals of T_I is used to detect the pulses.

Simplified block diagrams of these UWB non-coherent receivers are illustrated in Figures 3.1 (amplitude detection approach) and 3.2 (energy detection approach). The hardware front end design of such receivers will be further described in chapter 4.

3.2 Distance measurement procedure

The aim is to measure the distance between two UWB sensors by estimating the round-trip-time (RTT) of a UWB pulse which propagates between such sensors. One sensors is called master and the another is the slave. The is master is which actually measures the distance and controls the measurement procedure, while the slave is always waiting to receive pulses to respond to them. The same UWB non-coherent receiver (described in the previous section) is used in both sensors.

The distance is measured repeatedly with an update rate denoted by R_f. In this context, an update measurement rate of 100 Hz is desirable for accurate high dynamic range tracking. Let us denote the inverse of R_f by T_f, which is called in this document as frame duration. A frame is the time interval in which the master performs one distance measurement. Thus, the measurement procedure is repeated in every frame and it follows the following steps:

1. The master initiates the measurement procedure by sending a UWB pulse. It transmits a pulse at the beginning of every frame.

2. When the slave detects the pulse and it responds to the master after a fixed latency (T_w) by sending another pulse.

3. The master detects the slave response and it measures the RTT ($\hat{T}_{RTT}$) in order to estimate the distance.

It might happen that the master does not detect any pulse within a frame, so no distance estimation is given. In the next section, the probability of detection will be defined, which is the probability of having a distance estimation in a frame.

The process described above is the same for both amplitude and energy detection, only the technique to detect the pulse changes. Let us denote the following timing parameters related to the measurement process. Without loss of generality we do the analysis only considering one frame, for simplicity it starts at $t = 0$.

- T_f: Frame duration
- T_p: Propagation time. It is the elapsed time in the propagation of a pulse between the master and the slave, or viceversa. It is related to the distance by $T_p = \frac{d}{c}$, where the distance is denoted by d and c denotes the speed of light ($3 \cdot 10^8$ m/s).
- T_w: Slave latency. It is the elapsed time between the pulse reception at the slave and the response transmission.
- T_{ds}: Detection time at the slave. It is the time when the slave detects the pulse. Ideally, it would be T_p, but there may be an error.
- T_{RTT}: Round-trip time (RTT). It is the time when the pulse transmitted by the slave arrives to the master. $T_{RTT} = T_{ds} + T_w + T_p$, which ideally (considering that at the slave the pulse is detected without error, i.e. $T_{ds} = T_p$) would be $2T_p + T_w$.
- $\hat{T}_{RTT}$: Estimated RTT. It is the time when the master detects the pulse and it is used to measure the distance. Ideally, it would be T_{RTT}, but as in the detection at the slave there may be an error.

The estimated RTT, $\hat{T}_{RTT}$, is used to measure the distance between the master and the slave sensors. Thus,

$$\hat{d} = c\frac{\hat{T}_{RTT} - T_w}{2} \tag{3.1}$$

The above expression is valid if there is not an offset[1] in the error. To avoid that, a look-up table made with a previous calibration process can be used, as described in [1].

The RTT estimation may be any value within a frame due to the error at the slave or at the master. The measurement procedure and the timing parameters are illustrated in Figure 3.3. We can easily see that in this case the maximum distance which can be measured properly is bounded by the RTT. Therefore,

$$\begin{array}{c} T_{RTT}^{max} = T_f - T_b \\ T_p^{max} = \frac{T_{RTT}^{max} - T_w}{2} \\ d^{max} = c \cdot T_p^{max} \end{array} \tag{3.2}$$

Furthermore, the average power consumption due to the pulses transmission in both sensors would be $\frac{2E_b}{T_f}$. Thus, there is a trade-off between the measurement update rate, the range covered and the power consumption.

3.3 Theoretical analysis

In this section, more elaborated theoretical analysis of the RTT measurement process is provided.

The signal received by the slave is

$$r_s(t) = \sum_{j=-\infty}^{\infty} \sqrt{E_b} p(t - jT_f - T_p) + n(t) \tag{3.3}$$

where the frame index is denoted by j, E_b is the received pulse energy after amplification. Additive white Gaussian noise (AWGN) with zero-mean, double-sided power spectral density $\frac{\mathcal{N}_0}{2}$ and variance σ^2 is denoted by $n(t)$. Since the received signal is filtered, the bandwidth of the noise is limited. The variance or power of the noise is $\sigma^2 = \mathcal{N}_0 \cdot B$. The signal-to-noise ratio SNR is defined by $\frac{E_b}{\mathcal{N}_0}$. The UWB pulse of duration T_b is denoted by $p(t)$. Let us now denote the generic signal (it will be different for amplitude detection and energy detection) which is compared with a threshold, γ, at the slave by $y_s(t) = s_s(t) + v_s(t)$ where $s_s(t)$ is the pulse component and $v_s(t)$ is the noise component. Then, when $y_s(t)$ exceeds such threshold, the pulse is detected and the slave responds with another pulse after the latency, T_w.

[1] The offset of the error is equivalent to the error mean.

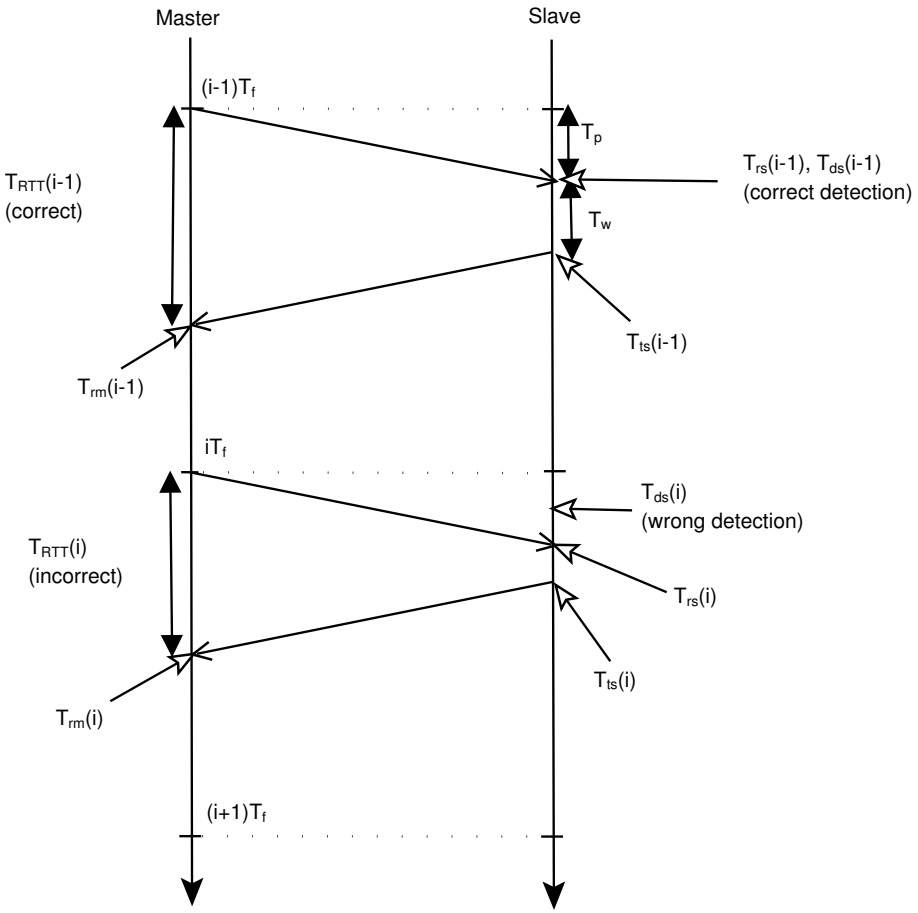

Figure 3.3: Timing diagram of the RTT estimation procedure. Two measurements are shown. In the (i-1)-th frame the pulse is correctly detected at the slave ($T_{rs} = T_{ds}$), while in the i-th frame the slave detects the pulse when it is not present due to the noise and consequently the RTT is wrong.

Without loss of generality we do the analysis within a single frame, for simplicity the one with index $j = 0$. Hence, the instant of the detection at the slave, T_{ds}, is given by

$$T_{ds} = \min_{y_s(t)>\gamma} \left(t \in [-T_w - T_p \,,\, T_f - T_w - T_p]\right) \tag{3.4}$$

what means that the first time instant when the signal crosses the threshold, producing a pulse which arrives to the master within the frame $j = 0$, is the slave detection instant. Thus, the signal received by the master is

$$r_m(t) = \sqrt{E_b} p(t - T_{RTT}) + n(t) \tag{3.5}$$

and the generic signal compared with a threshold at the master is $y_m(t) = s_m(t) + v_m(t)$, so the estimated RTT is

$$\hat{T}_{RTT} = \min_{y_m(t)>\gamma} \left(t \in [0 \,,\, T_f]\right) \tag{3.6}$$

The correct time of detection is assumed to be when the pulse component, $s(t)$, crosses the threshold, γ. Thus, if we denote such time instants for zero delay by t_1 and t_2 (with $t_1 < t_2$), we have that

$$s_s(T_p + t_1) = s_s(T_p + t_2) = s_m(T_{RTT} + t_1) = s_m(T_{RTT} + t_2) = \gamma \tag{3.7}$$

Therefore, the error at the master and at the slave, ξ_m and ξ_s, respectively, would be

$$\begin{aligned} \xi_m &= \hat{T}_{RTT} - T_{RTT} - t_1 \\ \xi_s &= T_{ds} - T_p - t_1 \end{aligned} \tag{3.8}$$

and the total error

$$\xi_t = \xi_m + \xi_s = \hat{T}_{RTT} - 2T_p - T_w - 2t_1 \tag{3.9}$$

Hence, we are interested in finding out the probability density function (PDF) of such error, $f_{\xi_t}(\xi)$. Let us denote the PDF of the estimated RTT, $\hat{T}_{RTT}$, given the actual RTT, by $f_{\hat{T}_{RTT}}(\tau; T_{RTT})$. The SNR, the shape and the threshold will also affect the distribution of such estimated RTT. Note that

$$\int_0^{T_f} f_{\hat{T}_{RTT}}(\tau; T_{RTT})\, d\tau = P_D \tag{3.10}$$

where P_D is the probability of detection at the master ($y_m(t)$ crosses the threshold at least once within the frame) with $0 \leq P_D \leq 1$, so it is not exactly a proper PDF. With the remaining probability, $P_M = 1 - P_D$, the pulse is not detected. Then, the PDF of T_{ds} given T_p is related to $f_{\hat{T}_{RTT}}(\tau; T_{RTT})$ by

$$f_{T_{ds}}(\tau_s; T_p) = f_{\hat{T}_{RTT}}(\tau + T_p + T_w; 2T_p + T_w) \tag{3.11}$$

If we denote now the PDF of $\hat{T}_{RTT}$, given T_p instead of T_{RTT} by $f'_{\hat{T}_{RTT}}(\tau_m; T_p)$, such PDF is related to $f_{\hat{T}_{RTT}}(\tau;\, T_{RTT})$ by

$$\begin{aligned} f'_{\hat{T}_{RTT}}(\tau_m; T_p) \;=\; & \left(\int_{-T_p-T_w}^{T_f-T_p-T_w} f_{\hat{T}_{RTT}}(\tau_m; \tau_s + T_w + T_p)\cdot \right. \\ & \left. f_{\hat{T}_{RTT}}(\tau_s + T_p + T_w; 2T_p + T_w)\, d\tau_s\right) \\ & + (1 - P_D)\, f_{\hat{T}_{RTT}}(\tau_m; T_f) \end{aligned} \tag{3.12}$$

Finally, the PDF of the total error can be expressed in terms of $f'_{\hat{T}_{RTT}}(\tau_m; T_p)$

$$f_{\xi_t}(\xi; T_p) = f'_{\hat{\tau}_{RTT}}(\xi + 2T_p + T_w + 2t_1; T_p) \tag{3.13}$$

The total probability of detection would be

$$P_D^T = \int_0^{T_f} f_{\hat{T}_{RTT}}(\tau_m; T_p)\, d\tau_m \tag{3.14}$$

With probability $P_M^T = 1 - P_D^T$ no RTT estimation is given. It can be approximated by $P_D^T = P_D^2$, considering that the detection at the master is independent to the detection at the slave. Thus, the effective measurement update rate could be expressed by $R_f^{eff} = P_D^T R_f$

Moreover, we can analyze the probability of false alarm and the probability of hit. This analysis is a bit different to the classical detection problem. We denote by $\mathcal{H}_1$, $\mathcal{H}_0$ the hypotheses "$s(t)$ exceeds the threshold" and "$s(t)$ does not exceed the threshold", respectively. A false alarm occurs when the pulse is detected but $\mathcal{H}_0$ is true, i.e. $y(t)$ crosses the threshold , but not $s(t)$ (the detection is due to the noise). On the other hand, a hit occurs when the pulse is detected and $\mathcal{H}_1$ is true, i.e. $s(t)$ crosses the threshold in the detection time. The false alarms will produce errors in the timing estimation.

$$\begin{array}{ccc} False\ Alarm\,(slave) & \rightarrow & T_{ds} \notin [T_p + t_1, T_p + t_2] \\ Hit\,(slave) & \rightarrow & T_{ds} \in [T_p + t_1, T_p + t_2] \\ False\ Alarm\,(master) & \rightarrow & \hat{T}_{RTT} \notin [T_{RTT} + t_1, T_{RTT} + t_2] \\ Hit\,(master) & \rightarrow & \hat{T}_{RTT} \in [T_{RTT} + t_1, T_{RTT} + t_2] \end{array} \tag{3.15}$$

If we denote these probabilities by P_{FA} and P_H, we have that $P_{FA} + P_H = P_D$. We can derive P_{FA}^S and P_H^S from $f_{T_{ds}}(\tau_s; T_p)$ by

$$P_H^S = P_D^S - P_{FA}^S = \int_{T_p+t_2}^{T_p+t_1} f_{T_{ds}}(\tau_s; T_p)\, d\tau_s \tag{3.16}$$

and equivalentlyP_{FA}^M and P_H^M from $f'_{\hat{T}_{RTT}}(\tau_m; T_p)$by

$$P_H^M = P_D^M - P_{FA}^M = \int_{T_p+t_2}^{T_p+t_1} f_{\hat{T}_{RTT}}(\tau_m; T_p)\, d\tau_m \tag{3.17}$$

These probabilities can be assumed to be equal, thus the probability of hit at both master and slave in the same frame can be approximated by $P_H^T = \left(P_H^S\right)^2$.

3.3.1 Amplitude Detection

In this case, the amplitude of the received signal is just compared with a threshold, γ_A, to decide whether the pulse is present or not. Hence, $y(t) = r(t)$, $s_s(t) = \sqrt{E_b}p(t - T_p)$, $s_m(t) = \sqrt{E_b}p(t - T_{RTT})$ and $v(t) = n(t)$. The block diagram is shown in Figure 3.1

The PDF of the received signal in absence of the pulse is the same as the noise PDF, i.e. Gaussian distribution with zero mean

$$f_{r(t)}(r(t); t \notin [\tau_{toa}, \tau_{toa} + T_b]) = \frac{1}{\sigma^2\sqrt{2\pi}} e^{-\frac{r^2(t)}{2\sigma^2}} \tag{3.18}$$

where τ_{toa} denotes the time of arrival (TOA) of the pulse to the corresponding sensor[2]. When the pulse is present it is a Gaussian distribution with non-zero mean

$$f_{r(t)}(r(t); t \in [\tau_{toa}, \tau_{toa} + T_b]) = \frac{1}{\sigma^2\sqrt{2\pi}} e^{-\frac{\left(r(t) - \sqrt{E_b}p(t - \tau_{toa})\right)^2}{2\sigma^2}} \tag{3.19}$$

The mean is $\sqrt{E_b}p(t - \tau_{toa})$, which obviously it varies over the time. Hence, the received signal, $r(t)$, is a Gaussian process with time-varying mean, i.e. it is not stationary.

Now, we want to find out an analytical expression for $f_{\hat{\tau}^A_{RTT}}(\tau; T_{RTT})$ in order to find the distribution of the total error, $f_{\xi_t}(\xi; T_p)$ (see the previous section). We could also find the CDF (cumulative distribution function) and compute its derivative in order to find the PDF. The CDF of $\hat{T}^A_{RTT}$ given T_{RTT}, can be written as follows

$$F^A_{\hat{T}_{RTT}}(\tau; T_{RTT}) = \Pr\left(\hat{\tau}^A_{RTT} \leq \tau\right) = 1 - \Pr\left(r_m(t; T_{RTT}) < \gamma_A; \forall t \in [0, \tau]\right) \tag{3.20}$$

We know that the "instantaneous" probability[3] of the received signal to be lower than a threshold is

$$\Pr\left(r_m(t; T_{RTT}) < \gamma_A\right) = 1 - Q\left(\frac{\gamma_A - \sqrt{E_b}p(t - T_{RTT})}{\sigma}\right) \tag{3.21}$$

where $Q(\cdot)$ is the right-tail probability function of the standard normal distribution. It is very complex to find a closed analytical expression for $F^A_{\hat{T}_{RTT}}(\tau; T_{RTT})$ due to the fact that the time is continuous. However, we can approximate the probability of detection, P_D as follows

$$P_D = 1 - \prod_{k=0}^{4\frac{T_f}{T_b}} \left[1 - Q\left(\frac{\gamma_A - \sqrt{E_b}p\left(k\frac{T_b}{4}\right)}{\sigma}\right)\right] \tag{3.22}$$

[2]The TOA is T_p in the slave and T_{RTT} in the master.

[3]Since the system is full-analog, we define a "instantaneous" probability as a probability at a certain time instant.

This approximation is based on the assumption of the fact that the noise at instant separated more than $\frac{T_b}{4}$ is independent, i.e the autocorrelation of the noise is zero for $t \geq \frac{T_b}{4}$. Such probability of detection depends on the frame duration (T_f), the pulse shape, the threshold (γ_A) and the SNR. This is the probability of detection only at one sensor, thus the total probability of detection can be approximated by $P_D^T = P_D^2$.

3.3.2 Energy Detection

In this case, the energy of the signal is compared with a threshold, γ_E, to decide whether the pulse is present or not. The energy of the signal is

$$y(t) = \int_{t-T_I}^{t} r^2(t)\, dt \tag{3.23}$$

where T_I is the time interval of integration in which the energy is computed and it is assumed that $T_I \geq 2T_b$. Moreover, the signal component and the noise component are

$$\begin{array}{c} s(t) = E_b \int_{t-T_I}^{t} p^2(t-\tau_{toa})\, dt \\ v(t) = \int_{t-T_I}^{t} \left(n^2(t) + 2\sqrt{E_b} p(t-\tau_{toa})\, n(t)\right) dt \end{array} \tag{3.24}$$

Where τ_{toa} is the TOA of the pulse to the corresponding sensor (T_p in the slave and T_{RTT} in the master). The block diagram can be found in Figure 3.2. The PDF of $y(t)$ in absence of the pulse is said to have a central chi-square distribution with $2T_I B$ grades of freedom [22], i.e.

$$y(t; t \notin [\tau_{toa}, \tau_{toa} + T_b + T_I]) \sim \frac{N_0}{2} \chi^2_{2T_I B} \tag{3.25}$$

This is only true with the assumption of $T_I \geq 2T_b$. When the pulse is present it is a non-central chi-square distribution with $2T_I B$ grades of freedom and non-centrality parameter given by

$$\lambda(t) = 2 \cdot SNR \int_{t-T_I}^{t} p^2(t-\tau_{toa})\, dt \tag{3.26}$$

which for $\tau_{toa} + T_b \leq t \leq \tau_{toa} + T_I$ is just $2 \cdot SNR$ because the whole pulse is covered by the integration interval.

In this case, the instantaneous probability of of the received signal to be higher than a threshold is

$$\Pr(y_m(t) > \gamma_E) = Q_{\chi^2_{2T_I B}(\lambda(t))}\left(\frac{2\gamma_E}{\mathcal{N}_0}\right) \tag{3.27}$$

where $Q_{\chi^2_\nu(\lambda)}(\cdot)$ is the right-tail probability of a non-central chi-square distribution with ν degrees of freedom and non-centrality parameter λ.

In this case, the probability of detection, P_D can be approximated by

$$P_D = 1 - \prod_{k=0}^{\frac{T_f}{2T_b}} \left[1 - Q_{\chi^2_{2T_I B}(\lambda(2T_b k))} \left(\frac{2\gamma_E}{\mathcal{N}_0} \right) \right] \tag{3.28}$$

which is based on the assumption on the fact that the noise component, $v(t)$, is independent at instants separated more than $2T_b$. Note that this interval for the independence is larger than in amplitude detection. This is due to the integration and it makes that energy detection is more robust against the noise.

3.4 Computing the threshold

One choice to select the threshold would be to compute it from 3.22 in the case of amplitude detection or from 3.28 for energy detection in terms of the detection probability requirements for a certain SNR. Thus, the threshold would be the highest to achieve a certain value of probability of detection and therefore, the accuracy of the estimation would be the optimum for such a SNR and probability of detection.

Another option is to compute the threshold in terms of the false alarm requirements, by setting the instantaneous probability of detection when only the noise is present, i.e. the "instantaneous" probability of false alarm, called as denoted by p_d. The expressions to compute the threshold by this method are given below. In this case, the threshold in terms of the SNR, but of the noise power.

Note that in order to use the methods described above, it is needed to know the actual noise power and the pulse energy in the case of the first method. Such noise power could be estimated using adaptive algorithms, such as those presented in. This flexible configuration leads to the convenient design and implementation of fast adaptive threshold setting algorithms, such as those presented in [23]. For simplicity, in this thesis we assume that the noise power is perfectly known at the receiver.

3.4.1 Amplitude detection

Since the statistical distribution of the received signal is known, the threshold for amplitude detection can be derived from (3.21) setting as zero the pulse component.

$$\gamma_A = \sigma Q^{-1}\left(p_d^A\right) \tag{3.29}$$

where p_d^A denotes the instantaneous probability of the only-noise signal to exceed the threshold and $Q^{-1}(\cdot)$ is the inverse right-tail probability function of the standard normal distribution. The noise power is σ^2.

3.4.2 Energy detection

As for amplitude detection, the threshold can be computed in terms of the noise power. Thus, once the noise power is known, setting the non-centrality parameter to zero in (3.27), the threshold can be computed in terms of the instantaneous probability of false alarm

$$\gamma_E = \frac{\mathcal{N}_0}{2} Q^{-1}_{\chi^2_{2TB}} \left(p_d^E \right) \tag{3.30}$$

where $Q^{-1}_{\chi^2_\nu}(\cdot)$ is the inverse rig-tail probability of a central chi-square distribution with ν degrees of freedom (a non-central chi-square distribution with zero non-centrality parameter is equivalent to a central chi-square distribution).

Chapter 4

UWB Non-Coherent Receiver Front End Design

This chapter describes the UWB front end design which has been performed in this thesis. The sensor architecture is based on the design from [1], and the focus has been made in the part of the receiver. Two designs were carried out, one for amplitude detection and another for energy detection and two boards were implemented for each design since the same design is used for both master and slave. The board design was made using the software Eagle.

4.1 Sensor architecture

The architecture of the sensor unit is shown in Figure 4.1. It is composed of an analog UWB measurement section, which was designed in-house and implemented using elementary off-the shelf components, and a digital processing section, which is based on a field programmable gate array (FPGA). Conceptually, the interface between the analog UWB section and the digital processing section is provided by a time-to-digital converter (TDC) commercial integrated circuit, which provides RTT measurements with a resolution of 65 ps. Furthermore, a 12-bit digital-to-analog converter (DAC) is programmed by the FPGA and used to set the threshold of the energy detector/comparator in the UWB receiver section. This flexible configuration leads to the convenient design and implementation of fast adaptive threshold sitting algorithms, such as those presented in [23]. Overall, the modular nature of this architecture enables the testing of alternative solutions both for the radio front end and the digital processing algorithms.

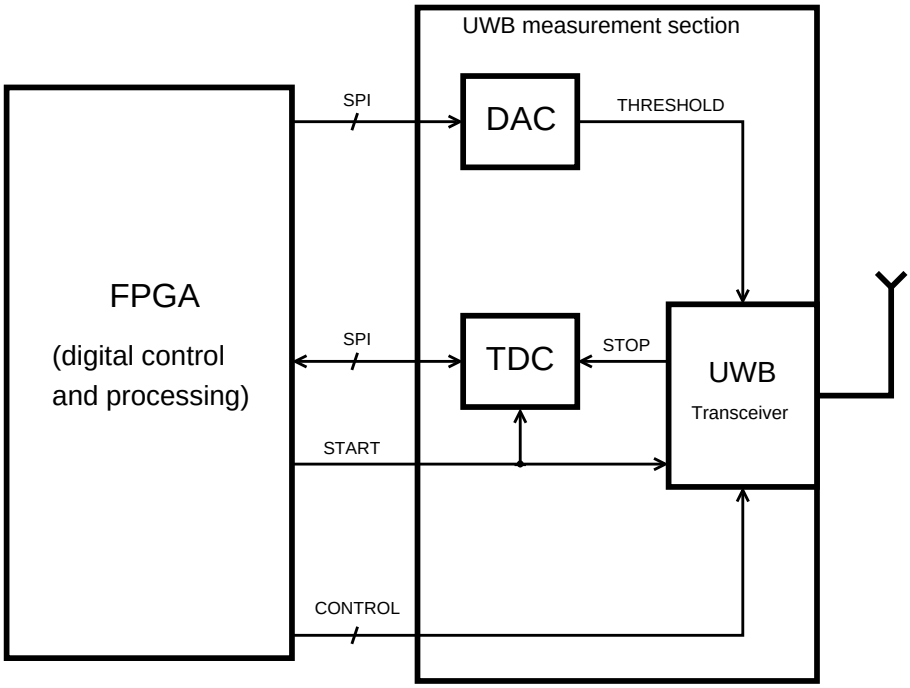

Figure 4.1: Simplified diagram of the architecture of the sensor unit. The analog UWB measurement section is connected to the FPGA using serial peripheral interface (SPI) connections to the TDC and the DAC for configuration. The connection between the TDC and the FPGA is also used to read the measured RTT values. The FPGA triggers and controls the UWB transceiver directly using digital control signals.

Two different UWB transceiver were implemented, using the non-coherent energy detection and amplitude detection approaches. Its main advantages are low-complexity and low-power implementation, because it avoids Nyquist-rate sampling of the UWB signal, which is infeasible for many applications due to the high bandwidth. Such transceiver section is illustrated by the block diagram in Figure 4.2. In such block diagram, a switch is used in order to use a single antenna, but in the final board it is also possible to use one antenna for transmission and another one for reception. The receiver part is different for amplitude or energy detection; the amplitude detection receiver uses just a comparator, while the energy detection receiver uses and energy detector (ED) which includes the square-law device, integrator and comparator (see Figure 3.2) in the same chip. Moreover, the design includes a low-noise amplifier (LNA) which is not included in the block diagram of Figure 4.2.

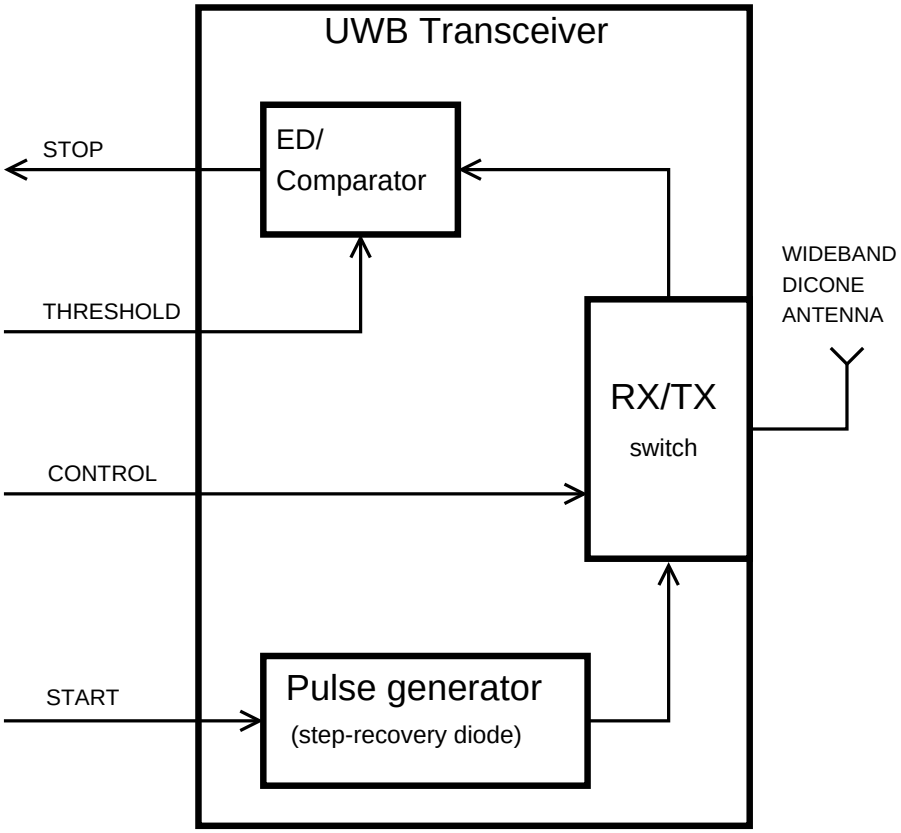

Figure 4.2: Architecture of the UWB transceiver. The pulse generator is realized using a step-recovery diode based on the circuit characterized in [24] and is triggered by the start signal from the FPGA. The output of the energy detector (ED)/comparator, after being compared with the voltage threshold in the on-chip comparator, provides the stop signal for the TDC measurement. The single-pole-double-throw (SPDT) switch selects the RX or TX position controlled by digital signals from the FPGA. A wideband omnidirectional discone antenna is used for the transmission and reception of the UWB pulses.

The digital section allows for implementing the proper timing and operation of the sensor system. In particular, as shown in Figure 4.1, the UWB measurement section requires various digital control and setup signals. The functionalities of the digital section are listed below:

- Controlling the UWB transmitter: The measurement is initiated when the master interrogates the slave by sending a UWB pulse. The trigger signal to the transmitter is generated digitally. It is possible to dynamically adjust the frame duration, T_f (update measurement rate).

- Configuring and controlling the TDC: the TDC is configured to perform the measurement. The TDC measurement is initiated when the pulse is transmitted. The TDC communicates through a SPI interface.

- Controlling the transmit/receive switch: The transmit and receive switch connection the antenna to the transceiver is controlled digitally.

- Configuring the DAC for the detection threshold: the value of the threshold to detect the pulse at the output of the ED/comparator is set digitally. It can be set a priori or can be calculated adaptively depending on the false alarm requirements.

- Post-processing for range estimation: Once the master receives the answer from the slave, it computes the range the RTT readings from the TDC.

In the digital processing section, the FPGA provides flexibility in the development, implementation and tuning of algorithms. ML505 Virtex-5 FPGA boards are used to implement the digital functionalities listed above. The FPGA allows reconfigurable control of the UWB front end.

4.2 Hardware: Selection of the components

The UWB measurement section was implemented as a printed circuit board on FR4 substrate with a thickness of 1.0 mm. A picture of the realized board is shown in Figure (**include picture**). As said before, in this thesis the effort in the design of the boards has been made in the receptor part, specially in the selection of the LNA, comparator and ED.

First, a search of components suitable for the design was made and then they were prioritized taking into account different features.

Table 4.1: Suitable LNAs for the receiver front end. The first column indicates the priority taking into account all the features, f_1 and f_2 are the low and high frequency of the operation bandwidth, respectively. B denotes the bandwidth of operation ($f_2 - f_1$), NF and G are the noise figure and the gain, respectively. The seventh columns indicates the supply current and the last two columns show the manufacturer and the device reference. The row in red is the LNA chosen for the design.

Pr.	f_1	f_2	B (GHz)	NF (dB)	G (dB)	S.C. (mA)	Manufact.	Manufact. ref.
1	400 MHz	1.5 GHz	1.1	0.66	31.8	45	Avago	MGA-13516
2	400 MHz	1.4 GHz	1	0.52	21.3	60	Freescale	MML09211H
3	5 MHz	2 GHz	1.995	1.1	20	5.2	RFMD	SGL0363
4	100 MHz	2.5 GHz	2.4	1.2	24	4.7	Freescale	MBC13917
5	400 MHz	2.5 GHz	2.1	1.2	20	5	Freescale	MBC13720
6	1 GHz	2.5 GHz	1.5	1.27	18.9	3.8	Freescale	MC13851
7	100 MHz	1.5 GHz	1.4	1	19.7	10	Avago	MGA-68563
8	500 MHz	1.7 GHz	1.2	0.4	17.7	50	Avago	MGA-16516
9	45 MHz	2.5 GHz	2.455	1.5	15	6	RFMD	RF2884
10	450 MHz	2 GHz	1.55	0.56	17.8	40	Avago	MGA-683P8
11	100 MHz	1.3 GHz	1.2	1.2	15.5	12	RFMD	SGL0163Z
12	400 MHz	4 GHz	3.6	0.8	21	30	Analog	ADL5523ACPZ
13	500 MHz	2.5 GHz	2	1.5	19	12	RFMD	RF2442
14	800 MHz	2.4 GHz	1.6	1.55	13.5	7.8	Freescale	MC13853
15	150 MHz	2.5 GHz	2.35	1.4	12.9	5.7	RFMD	RF2314
16	50 MHz	4 GHz	3.95	0.8	18.2	46	RFMD	SPF5043Z
17	0	4 GHz	4	1.9	24	45	RFMD	SGA4586Z
18	300 MHz	2.5 GHz	2.2	1.6	11.7	8	RFMD	RF2304

4.2.1 LNA

The LNA must operate in a wide band suitable for the used UWB pulse (see Table 2.1), but such bandwidth is also desirable to be as low as possible in order to reduce the noise. Furthermore, low noise figure (NF) and high gain are desired, as well as low current consumption. A noise figure of about 1 dB is considered good enough. Thus, some suitable LNAs are shown in Table 4.1 with some of its main features (bandwidth of operation, noise figure, gain and supply current), which are taken all into account in order to select the most adequate device. Since the pulse shape which will be used in the experiments is the Scholtz's monocycle, the LNA must operate within the bandwidth of such shape (see Table 2.1). That is not the case of the three first components. The fourth one was not available by the supplier, so finally the LNA MBC13720

Table 4.2: Parts list

Component	*Part number*
TDC	TDC-GP2, Acam Messelectronic
DAC	ADC5620, Analog Devices
Pulse generator diode	5082-0112, HP
Switch	RSW-2-25P, Mini Circuits
LNA	MBC13720, Freescale Semiconductor
Comparator	LT1720, Linear Technology
Energy detector	LTC5536, Linear Technology

from Freescale was selected. This LNA has adequate noise figure, gain and operation bandwidth, and the supply current is extremely low. Furthermore, the IP3 is 10 dBm at 1.9 GHz, which is acceptable.

4.2.2 Comparator

The comparator is used in the design of the non-coherent receiver for amplitude detection, but not in energy detection because one single integrated circuit includes the square-law device, the integrator and the comparator itself. We need a comparator as fast as possible (i.e. low response time) and with low supply current. Another requirement is the match between the logic output of the comparator and the input of the TDC. Such TDC requires a low level input voltage lower than 0.8 V and a high level input voltage higher than 2 V. Thus, some ultra-fast comparators with RSPECL outputs are not acceptable and we need a device with outputs which directly interface to TTL and CMOS inputs. Such comparators are slower, but they can be fast enough. Hence, the selected comparator was the LT1720 from Linear Technology, which has rail-to-rail outputs, 4.5 ns response time and 4 mA current consumption.

4.2.3 ED

The energy detector is equivalent to the comparator for the energy-detection receiver. The LTC5536 from Linear Technologies, which was also used in the previous design described in [1], was selected. This device rail-to-rail outputs, 25 ns response time and low operating current (2 mA).

4.3 Final design

A list of the main parts used in the UWB measurement boards is provided in Table 4.2.

Two LNAs were connected in cascade in the receiver in order to increase the sensitivity of the receiver. The schematics of both detectors are shown in Figures 4.3 and 4.4. Note that at the input and output of the LNAs there are networks

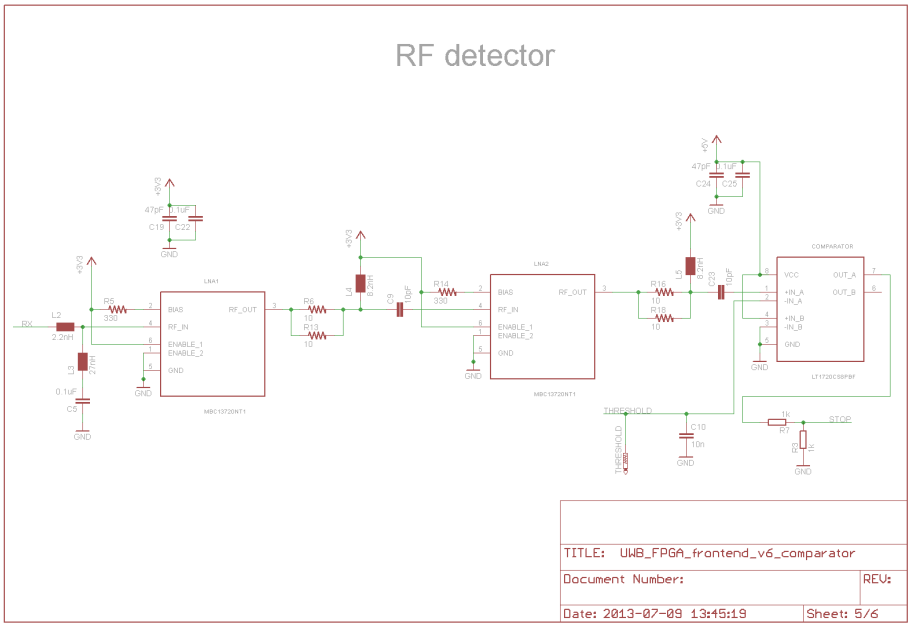

Figure 4.3: Schematic of the receiver with amplitude detection.

with passive components. Such networks were taken from the datasheet of the MBC13720 component [25] for a typical 900 MHz LNA application. Such networks implement a band-pass filter. The total transfer function of the filter (input and output of the LNA) is illustrated in Figure 4.5. The insertion loss is about 6 dB and the bandwidth is suitable for the design (considering Scholtz's monocycle shape).

Furthermore, the layouts of the whole boards of the measurement sections for both non-coherent receivers are illustrated in Figures 4.6 and 4.7. The final implemented boards are shown in Figures (4.8) and (4.9), for amplitude and energy detection, respectively.

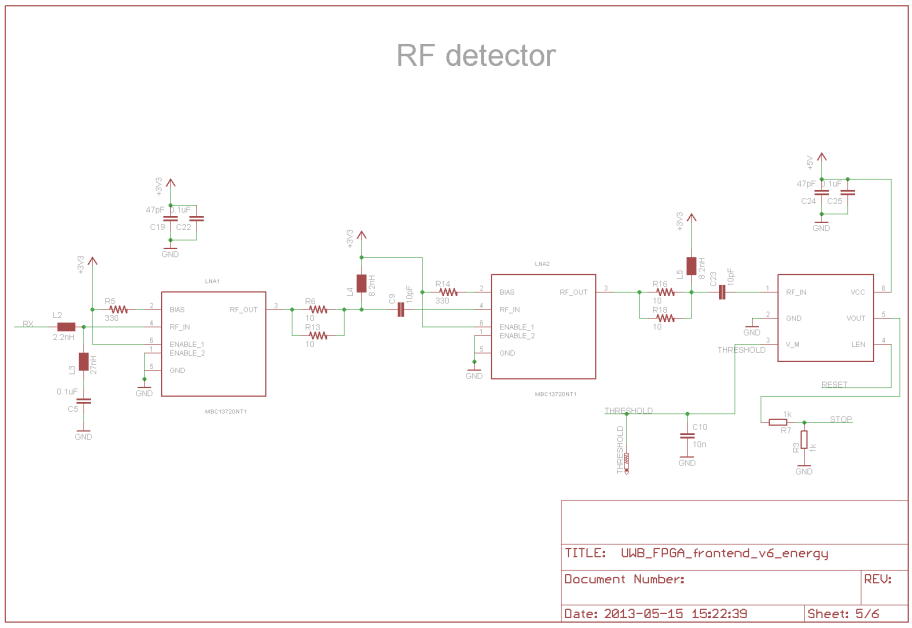

Figure 4.4: Schematic of the receiver with energy detection.

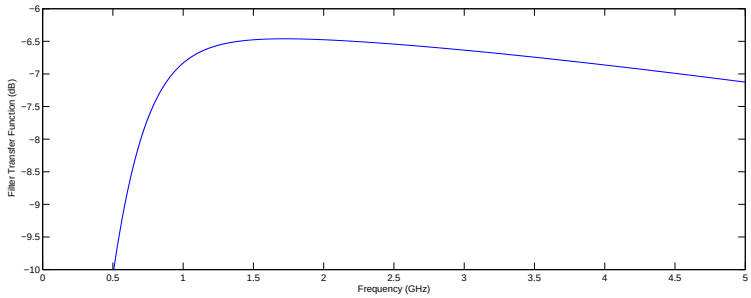

Figure 4.5: Frequency response of the filter

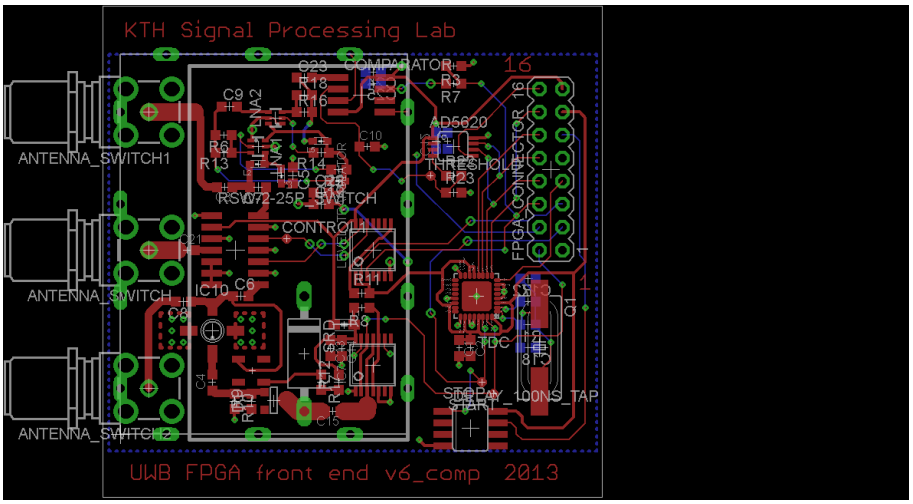

Figure 4.6: Board layout for amplitude detection.

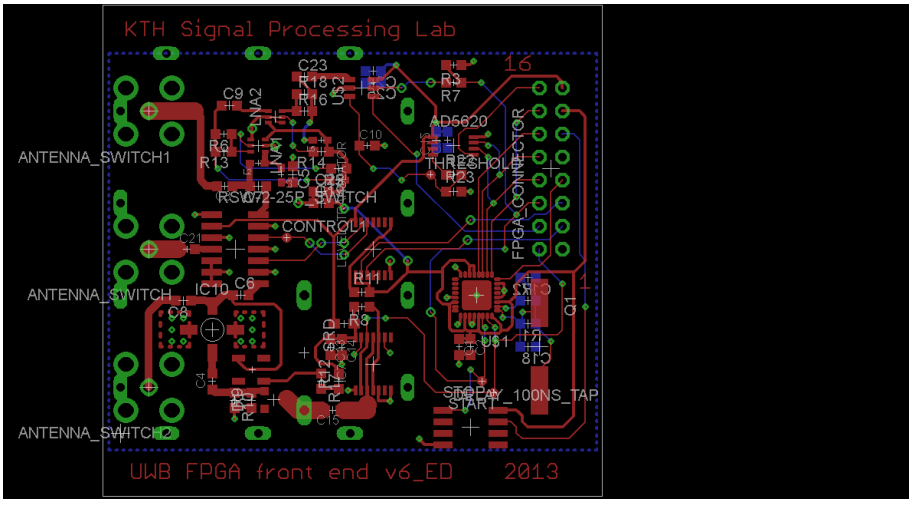

Figure 4.7: Board layout for energy detection.

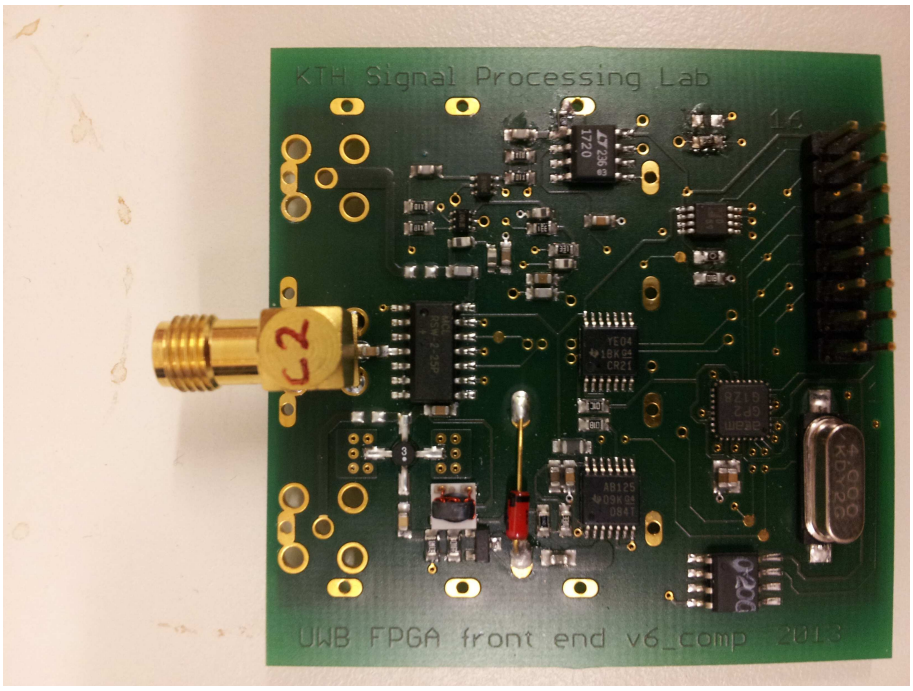

Figure 4.8: Implemented board for amplitude detection.

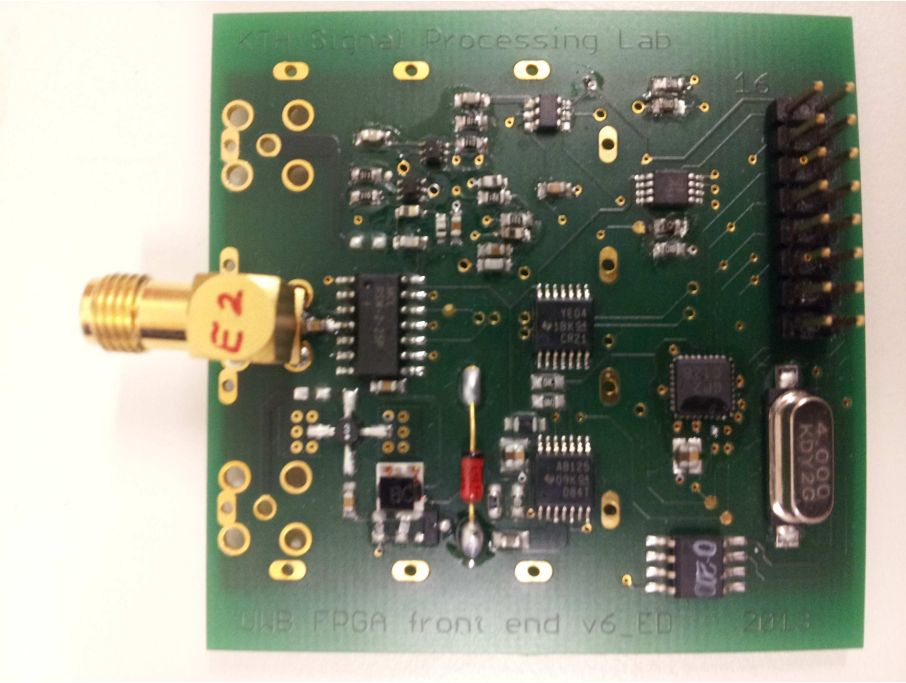

Figure 4.9: Implemented board for energy detection.

Chapter 5

Simulations Results

This chapter presents the simulations performed in this thesis using the software MATLAB. The performance of the RTT measurement has been simulated using the two different studied non-coherent UWB receivers, as well as the different UWB pulse shapes presented in section 2.1. Furthermore, the ideal UWB receiver has been also simulated in order to set its ideal performance as a boundary and compare it with the implemented non-coherent UWB receivers. Two performances types are considered for the analysis: accuracy performance and detection performance. In order to measure such performances, the error variance in the estimated RTT and the probability of detection (P_D^T in the theoretical description of chapter 4) are computed. The error variance is related to the accuracy, i.e. the lower the variance is, the more accurate is the estimation. Such statistical characteristics are computed by the repetition of the measurement process throughout a large enough number of iterations. Curves of the error variance and the probability of detection in terms of different parameters (SNR, threshold, etc.) are provided. Therefore, the performance for a certain scenario[1] is computed as follows

$$\mu_{\xi_t} = \frac{1}{N_i} \sum_{i=1}^{N_i} \xi_t (i) \tag{5.1}$$

$$\sigma_{\xi_t}^2 = \frac{1}{N_i} \sum_{i=1}^{N_i} (\xi_t (i) - \mu_{\xi_t})^2 \tag{5.2}$$

$$P_D^T = \frac{1}{N_i} \sum_{i=1}^{N_i} D (i) \tag{5.3}$$

[1] A scenario is mainly composed of the SNR, the pulse shape, the threshold, the frame duration and the propagation time (i.e. the distance).

Where μ and σ^2 denote the mean and variance of the error, respectively, the number of iterations is denoted by N_i and $D(i)$ is 1 if a RTT estimation is given in the i-th iteration or 0 otherwise. Following the same notation of the previous chapters, $\xi_t(i)$ denotes the total error of the estimated RTT in the i-th iteration.

The distance estimation error variance can be related to the RTT error variance as

$$\sigma_d^2 = c^2 \sigma_{\xi_t}^2 \tag{5.4}$$

Furthermore, the fixed latency of the slave, T_w, has been usually considered for simplicity zero several simulations in order to reduce the execution time. In practice, such latency is typically in the order of milliseconds, which is much larger than the actual propagation time, thus the signal to be simulated would be too large and consequently the execution time would be much longer. Thus, the simulations with zero slave latency are not actually reliable, but they are still useful for this investigation. However, some simulations have been carried out with non-zero latency time in order to show the influence of such latency. Thus, a curve illustrates the accuracy in terms of T_w. Moreover, the pulse duration was chosen to be 1 ns, and the noise is AWGN and low-pass with bandwidth $\frac{1}{T_b}$ for all the UWB pulse shapes.

In this context, a scenario is composed of the following parameters:

- Receiver type (ideal receiver, non-coherent receiver with amplitude detection, non-coherent receiver with energy detection)
- UWB pulse shape (see section 2.1)
- SNR, defined as $\frac{E_b}{\mathcal{N}_0}$.
- Threshold (γ_A and γ_E for amplitude and energy detection, respectively), computed from (3.29) for amplitude detection and from (3.30) for energy detection as a function of the noise power and p_d^A (amplitude) or p_d^E (energy). In the case of the ideal receiver, the threshold is computed as a percentage of $\sqrt{E_b}$, being E_b the pulse energy.
- Frame duration, T_f. It is the pulse repetition period and the inverse of the update measurement rate (R_f). It sets the maximum propagation time which can be measured properly: $T_p^{max} = \frac{T_f - T_w}{2}$
- Propagation time, T_p, related to the distance.
- Latency time for the slave to respond, T_w. It is the elapsed time between the pulse arrival and the slave response.
- Time of integration, T_I (only for energy detection).

5.1 Ideal UWB Receiver

In this section the simulations corresponding to the ideal UWB receiver are presented. The ideal receiver is described in section 2.2. This is used as a boundary to compare its performance with the non-coherent receivers. It is expected that the higher the sampling rate is, the better the performance will be. Due to the time restrictions, only the simulations corresponding to a sampling frequency of 30 GHz have been carried out, which is quite higher than the Nyquist-rate. The use of this sampling rate is not feasible in practice, but it is possible to simulate it and it can be useful for the comparison with the simulation of the implemented non-coherent receivers.

Thus, Figure 5.1 shows the probability of detection of the simulated ideal receiver for different thresholds[2] using the Scholtz's monocycle shape. We can observe that the detection performance is different for the different thresholds; $\gamma = 0.5\sqrt{E_b}$ seems to be suitable since even for SNR=0 dB, the probability of detection is high. Moreover, Figure 5.2 illustrates the error variance in terms of the SNR for $\gamma = 0.5\sqrt{E_b}$. The frame duration in this simulation is 150 ns, being the slave latency $T_w = 50\,ns$. We can see that the accuracy performance improves when increasing the SNR and it seems that there is not a boundary, in contrast to the performance of non-coherent detectors, as it will be shown in the corresponding simulations.

5.2 UWB Non-Coherent Receivers

This section presents the simulations corresponding to the UWB non-coherent receivers, i.e. amplitude detection and energy detection.

Thus, each scenario is simulated over $N_I = 500000$ iterations, computing the total error in the estimated RTT and then using (5.1), (5.2) and (5.3) in order to calculate the statistical results of the scenario simulation. The propagation time, T_p, is usually random for each iteration, i.e. the result is averaged over all the possible values of T_p. Thus, in the following illustrated simulations, unless the contrary is specified, T_p has been taken random for each iteration.

In the following subsections, the main results of the simulations of the RTT estimation using the UWB non-coherent receivers are presented.

[2]The threshold is computed as a percentage of $\sqrt{E_b}$. It is assumed that the received pulse energy is known.

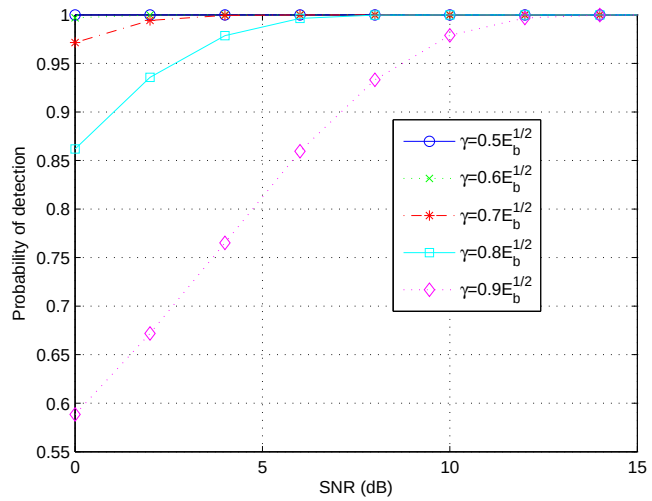

Figure 5.1: Probability of detection for ideal receiver with $T_f = 150\,ns$, random T_p and $T_w = 50\,ns$ in terms of the SNR. Each curve corresponds to a threshold. The used pulse shape is Scholtz's monocycle.

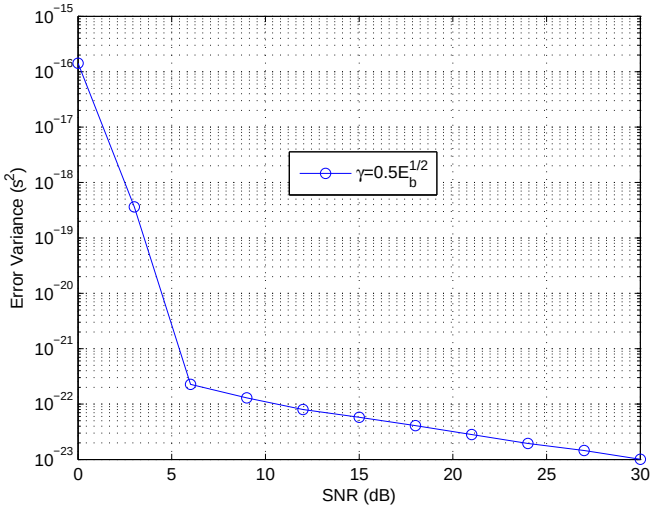

Figure 5.2: Error variance for ideal receiver with $T_f = 150\,ns$, random T_p and $T_w = 50\,ns$ in terms of the SNR. The used pulse shape is Scholtz's monocycle.

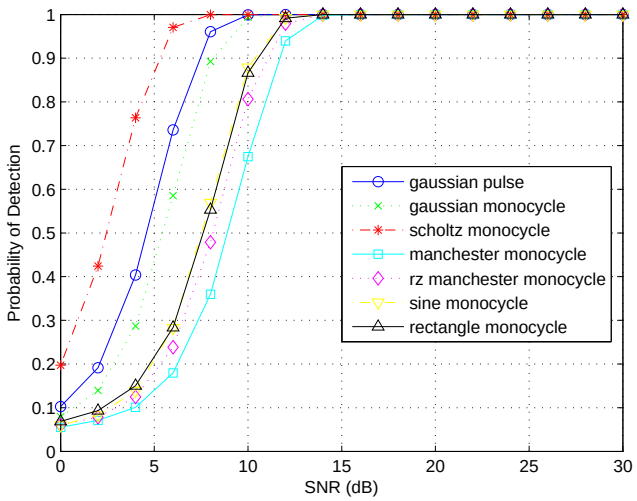

Figure 5.3: Probability of detection for amplitude detection with $p_d^A = 10^{-3}$, $T_f = 50\,ns$ and random T_p, in terms of the SNR. Each curve corresponds to a UWB pulse shape.

5.2.1 Detection performance: amplitude vs energy vs pulse shapes

Figure 5.3 shows the curves detection performance for amplitude detection for the all the considered UWB pulse shapes in terms of the SNR. The frame duration is 50 ns and the threshold is computed with $p_d^A = 10^{-3}$. The curves of the detection performance are different for the different shapes . Such difference is due to the fact that the different pulse shapes have different amplitude for the same energy and pulse duration (see Table 2.1), i.e. the higher the energy is for the same amplitude, the better the detection performance is. Hence, Scholtz's monocycle presents the best detection performance using amplitude detection.

On the other hand, the detection performance for energy detection is quite similar for all the pulse shapes (see Figure 5.4) because in this case what is compared with a threshold is the energy and for it is the same for the same SNR in all the pulses. The same parameters as the last simulations for amplitude detection are used in these simulations with energy detection.

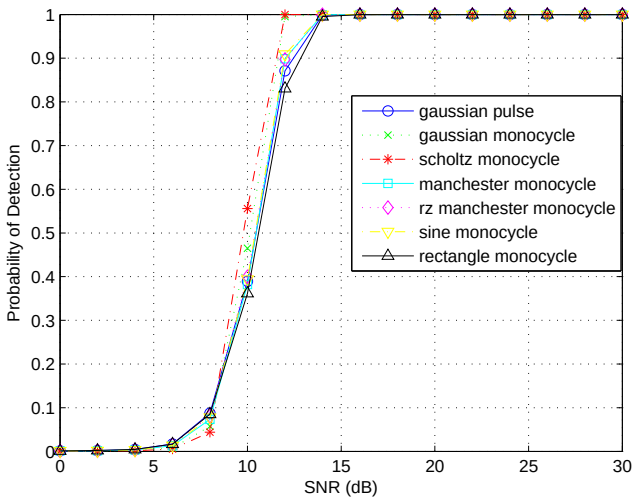

Figure 5.4: Probability of detection for energy detection with $p_d^E = 10^{-3}$, $T_f = 50\,ns$ and random T_p, in terms of the SNR. Each curve corresponds to a UWB pulse shape.

Moreover, we can check the validity of the approximations of the probability of detection presented in chapter 3 in expressions 3.22 and 3.28. Figure 5.5 shows the curves of the probability of detection of the simulations together with the theoretical curves. The theoretical approximations fit quite well the simulations, specially for amplitude detection. For energy detection, the matching between the approximation and the simulation is not so accurate, but is still a good approximation.

We desire a high probability of detection, nearly 1 if it is possible. Thus, from the detection performance curves, we can measure such performance as the required SNR to achieve a certain value for the probability of detection.

Comparing both receivers (with the thresholds computed with the same p_d), we can see that Manchester monocycle, RZ-Manchester monocycle, rectangular monocycle and sine monocycle present similar detection performance with both receivers (the SNR required to achieve probability of detection nearly 1 is similar), while Gaussian pulse, Gaussian monocycle and Scholtz's monocycle work better with amplitude detection regarding the detection performance. Figure 5.6 shows the detection performance curves of amplitude detection and energy detection (only Scholtz's monocycle for energy detection) together. Scholtz's monocycle requires lower SNR (for amplitude detection) to achieve probability of detection nearly 1 than the others pulse shapes.

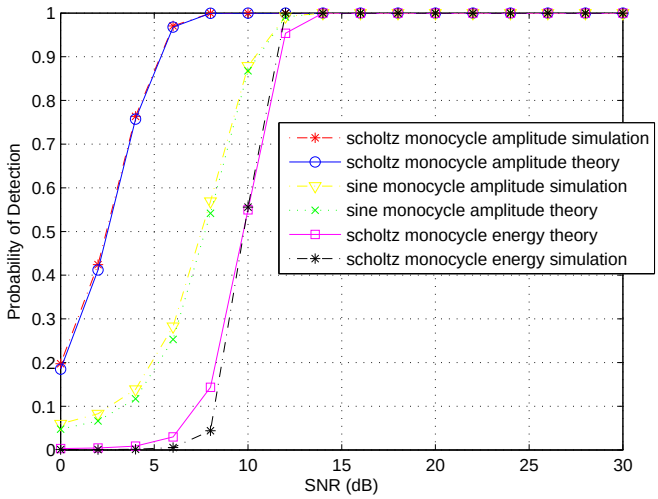

Figure 5.5: Comparison of the theoretical probability of detection and the probability of detection given by the simulations with $p_d = 10^{-3}$.

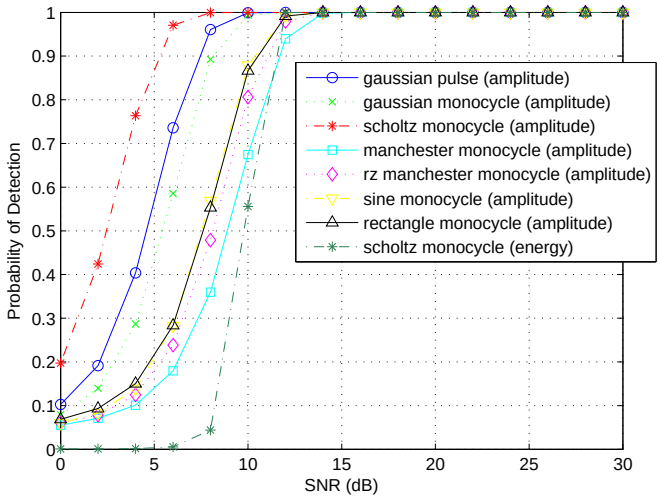

Figure 5.6: Probability of detection for amplitude detection (all shapes) and energy detection (only Scholtz's monocycle) with $p_d = 10^{-3}$, $T_f = 50\,ns$ and random T_p, in terms of the SNR. Each curve corresponds to a UWB pulse shape.

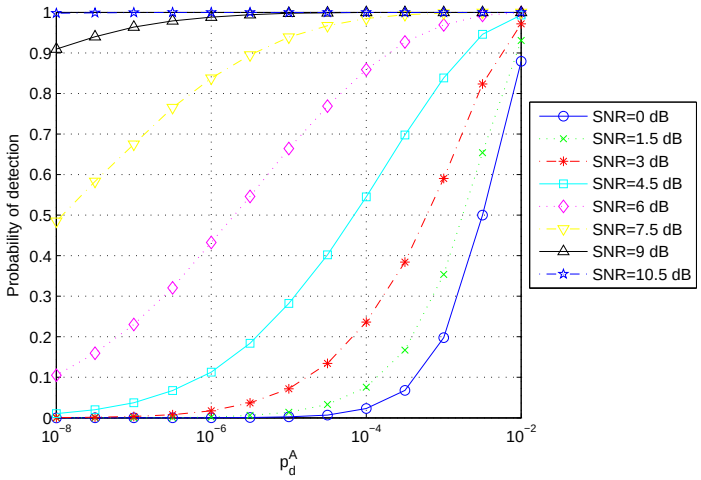

Figure 5.7: Probability of detection for amplitude detection using Scholtz's monocycle, $T_f = 50\,ns$ and random T_p, in terms of the threshold (p_d^A). Each curve corresponds to a certain SNR.

It is also worth to note that the detection performance of sine monocycle and rectangle monocycle is very similar with amplitude detection although sine monocycle has higher amplitude than rectangle monocycle for the same energy and pulse duration. The reason is that rectangle monocycle has the same amplitude during the whole pulse width while the amplitude in the sine monocycle varies over the pulse width and it is also negative within the half of the pulse width.

The same behavior yields with another thresholds, but more SNR is needed if the threshold is increased in order to achieve the same probability of detection. Figures 5.7 and 5.8 show the detection performance in terms of the threshold (p_d) for amplitude and energy detection, respectively, using Scholtz's monocycle. These curves are useful to see which threshold we can use with a certain value of SNR, yielding a good probability of detection. We will see in the following subsection that the accuracy is also related to the threshold and that higher threshold yields higher accuracy. Therefore, from Figures 5.7 and 5.8 we can see the highest threshold (or lowest p_d) which can be used for a certain SNR to provide a good probability of detection.

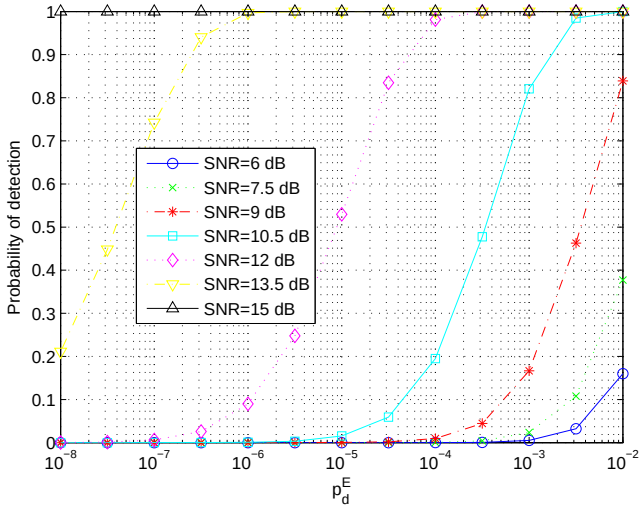

Figure 5.8: Probability of detection for energy detection using Scholtz's monocycle, $T_f = 50\,ns$ and random T_p, in terms of the threshold (p_d^E). Each curve corresponds to a certain SNR.

5.2.2 Accuracy: amplitude vs energy

The accuracy of the measurement is directly related to the threshold. The higher the threshold (lower p_d) is, the better the accuracy is. However, as we have seen in the previous subsection that the threshold also affects to the detection performance. Therefore, there exists a trade-off between the detection performance and the accuracy when we set the threshold.

For both energy and amplitude detection, there is a boundary for the accuracy that cannot be improved even if we increase more and more the SNR. This is due to the false alarms which occur during the elapsed time until the pulse arrives when the received signal is only noise. Such boundary is directly related to the threshold, the frame duration and the latency at the slave and the used pulse shape does not affect. The shape only affect for low SNR, for which the probability of detection is low. Figures 5.7 and 5.8 show the accuracy in terms of the threshold (p_d) for amplitude and energy detection, respectively using Scholtz's monocycle.

In Figure 5.11 the accuracy curves for both receivers are shown together, being p_d equal for both and using Scholtz's monocycle. For high SNR the accuracy is quite better with energy detection, but for low SNR amplitude detection is better (because amplitude detection requires lower SNR in order to achieve total detection).

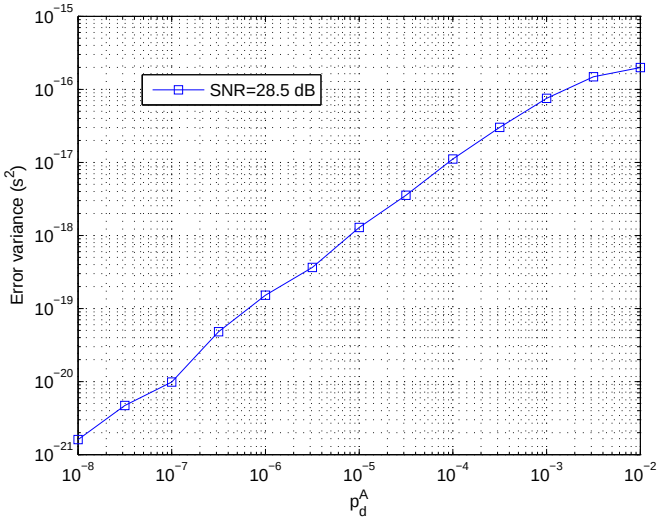

Figure 5.9: Error variance for amplitude detection using Scholtz's monocycle, $T_f = 50\,ns$ and random T_p, in terms of the threshold (p_d^A).

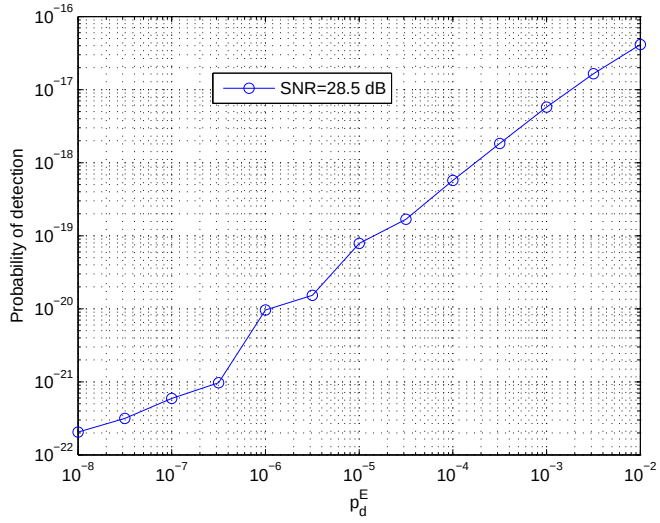

Figure 5.10: Error variance for energy detection using Scholtz's monocycle, $T_f = 50\,ns$ and random T_p, in terms of the threshold (p_d^A). Each curve corresponds to a certain SNR.

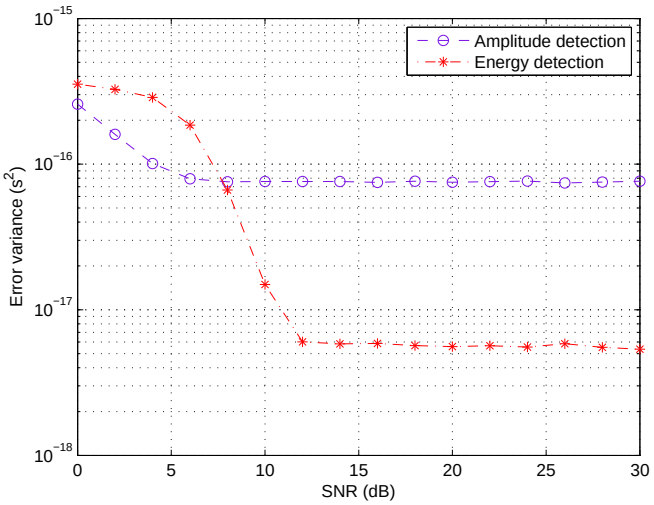

Figure 5.11: Comparison of the error variance for amplitude and energy detection, with $p_d = 10^{-3}$, $T_f = 50\,ns$ and random T_p, in terms of the SNR.

5.2.3 Influence of the propagation time and slave latency

The best accuracy that can be achieved is related to the time elapsed until the pulse arrives, because as longer is such elapsed time, as more probable is to have a false alarm. Thus, in the same conditions, the accuracy will be better with shorter propagation time (or shorter distance), which is shown in Figures 5.12 and 5.13 for amplitude and energy detection, respectively. However, the detection performance is the same. It is worth to note that the slope is higher for amplitude detection than for energy detection[3], i.e. the propagation time affects more to amplitude detection than to energy detection. Therefore, to support longer range it may be better to use energy detection.

For the same reason, the latency at the slave to respond will also affect the accuracy performance. Figure 5.14 shows the error variance in terms of T_w for both amplitude and energy detection. As it has been explained before for the propagation time, the deterioration due to the latency increase is higher for energy detection than for amplitude detection.

[3]Note that the y-axis is shown in logarithmic scale and it seems that the slope is similar for both amplitude and energy detection, but actually it is higher for amplitude detection

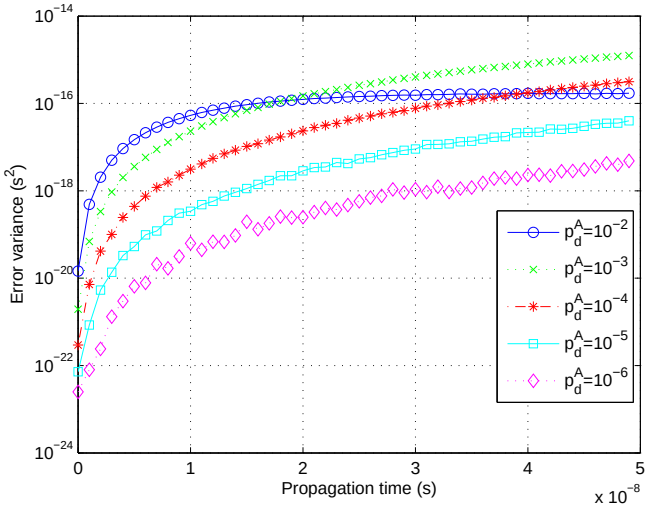

Figure 5.12: Error variance for amplitude detection using Scholtz's monocycle in terms of the propagation time, with $T_f = 100\,ns$ and $SNR = 16\,dB$. Each curve corresponds to a different threshold.

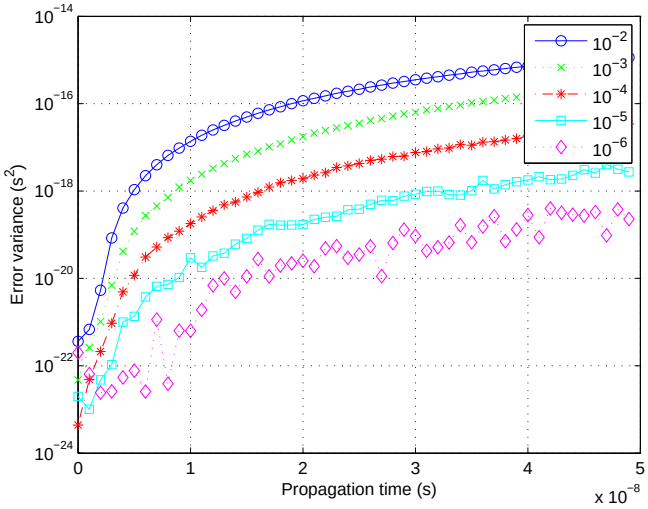

Figure 5.13: Error variance for energy detection using Scholtz's monocycle in terms of the propagation time, with $T_f = 100\,ns$ and $SNR = 16\,dB$. Each curve corresponds to a different threshold.

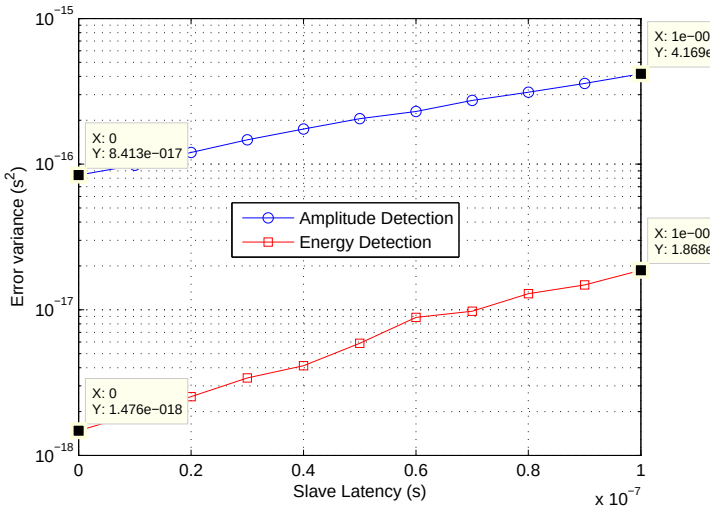

Figure 5.14: Error variance for energy detection and amplitude detection using Scholtz's monocycle in terms of T_w, with $T_p^{max} = 50\,ns$ and $SNR = 15\,dB$. Each curve corresponds to a detection technique.

5.2.4 Influence of the integration interval for energy detection

The accuracy of the measurements improves with longer integration intervals (see Figure 5.15). The reason is that in energy detection the noise is averaged, thus with longer integration the output of the integrator varies less. However, if the integration interval is too large, it may be very slow. Therefore, the value used in the previous simulations, $T_I = 5\,ns$ is considered suitable.

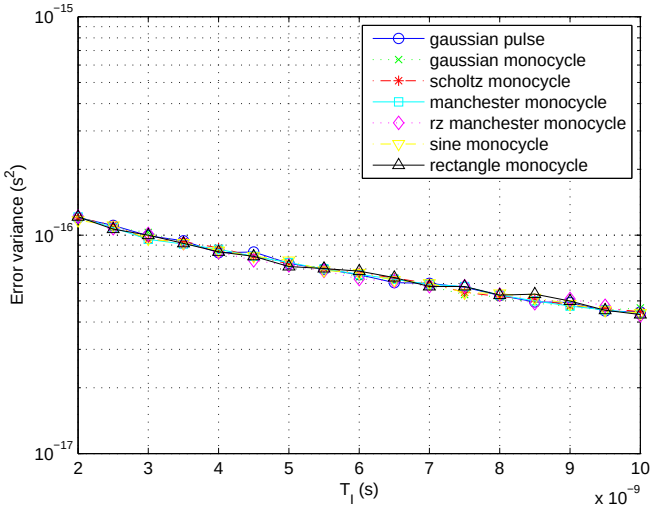

Figure 5.15: Error variance for energy detection in terms of the integration interval, with $T_f = 100\,ns$ and $SNR = 16\,dB$. Each curve corresponds to a different pulse shape.

Chapter 6

UWB Ranging with Undersampling Receiver

This chapter presents a proposed receiver which allows the sampling of the UWB pulse with a very low sampling rate compared with the Nyquist rate by the transmission of a burst of pulses. The aim is to try to approximate the performance of the ideal receiver described in section 2.2, but without the complexity given by the required high sampling rate.

6.1 Principle of operation

It may be used with the TOA approach (with the requirement of the synchronization) or with the RTT technique. If RTT is used, at the slave the detection should be a non-coherent approach (chapter 4), so this receiver could only be used at the master. Using such RTT method, the signal received by the slave would be the same as with the UWB non-coherent receivers. However, when the slave detects the pulse, it would respond with a burst of pulses with a constant delay between them. Thus, let the signal received at the master for the frame $j = 0$ be expressed as

$$r_m(t) = \sum_{i=0}^{N_p-1} \sqrt{E_b} p(t - iT_d - T_{RTT}) + n(t) \tag{6.1}$$

where T_d is the delay between consecutive pulses and N_p is the total number of transmitted pulses. The RTT is the time when the first pulse arrives to the master. The delay is given by

$$T_d = t_s - T_b/N_s \tag{6.2}$$

where t_s is the employed sampling rate, and N_s is the number of samples of the reconstructed pulse, i.e. it sets the resolution in the reconstructed pulse. There is a very low difference between the delay between pulses, T_d, and the

sampling rate, t_s (specifically such difference is just the required resolution in the reconstructed pulse). This is the same as saying that there is a *"jitter"* between the clock that controls the burst transmission and the clock used for sampling. This *"jitter"* allows the reconstruction of the pulse by undersampling the burst, since the relative position of the sampling instants and its closest pulse is changing over the time. In order to ensure the reconstruction of the pulse, the minimum number of pulses must be

$$N_p = \frac{(T_{RTT}^{max} + T_b)\, N_s}{T_b} + 1 \tag{6.3}$$

With such number of pulses, N_s samples will always be taken from the pulse if the RTT is not higher than T_{RTT}^{max}. Figure 6.1 illustrates a simple example of how the undersampling allows to reconstruct the pulse shape from the burst and Figure 6.2 shows the burst transmission and the sampling in a timing diagram. The maximum RTT is a parameter related to the maximum distance which we want to measure and there is a trade-off with the measurement update rate. Such $T_{RTT}^{max} = t_s - T_b$ is bounded by

$$T_w < T_{RTT}^{max} \leq t_s - T_b \tag{6.4}$$

And the maximum propagation time is

$$T_p^{max} = \frac{T_{RTT}^{max} - T_w}{2} \tag{6.5}$$

Furthermore, the required time to perform one measurement, i.e. the frame duration, is

$$T_f = t_s \cdot N_p \tag{6.6}$$

So if we want to maintain the same measurement range as with the ideal receiver, the measurement update rate must be reduced. The power consumption required to transmit all the pulses is $\frac{(N_p+1)E_b}{T_f}$, which is quite higher than with the ideal detector or the non-coherent detector with the same update measurement rate.

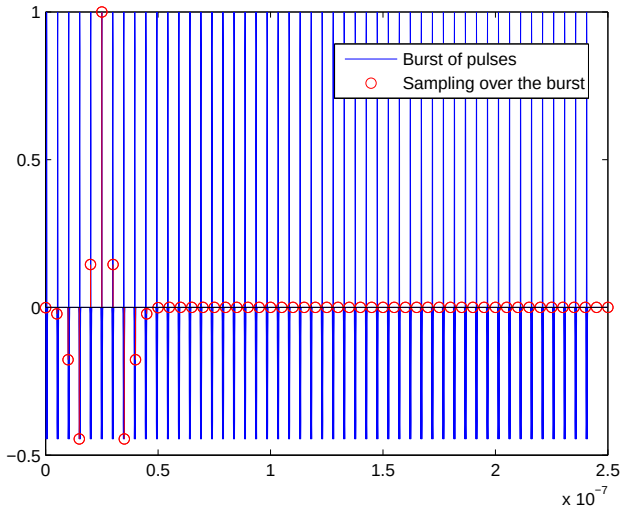

(a) $T_{RTT} = 0\,ns$

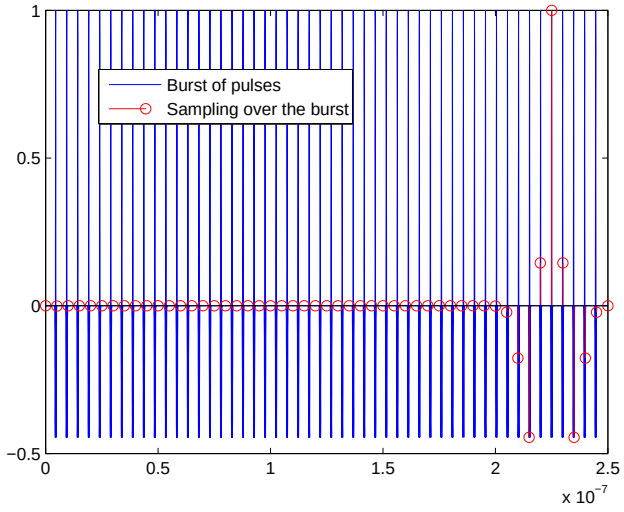

(b) $T_{RTT} = 4\,ns$

Figure 6.1: Simple example of how the sampling of the burst reconstructs the original pulse. The used UWB pulse shape is Scholtz's monocycle. The pulse duration, sampling rate and the number of samples per reconstructed pulse have the following values: $T_b = 1\,ns$, $t_s = 5\,ns$, $N_s = 10$. (a) $T_{RTT} = 0\,ns$, (b) $T_{RTT} = 4\,ns$.

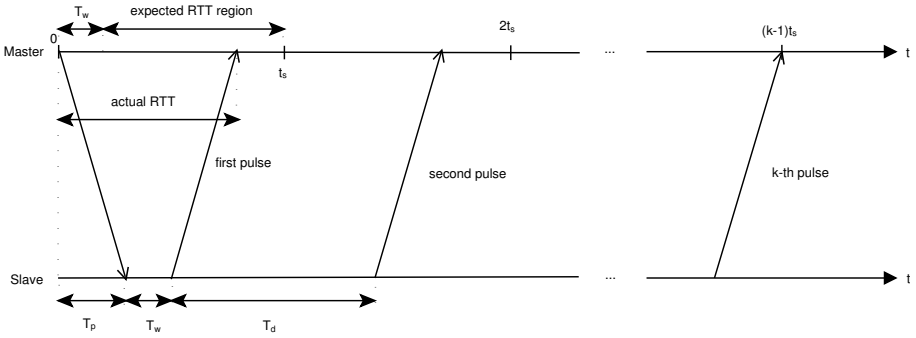

Figure 6.2: Timing diagram of the RTT measurement procedure using undersampling.

The sampled received signal is

$$r_m[n] = r_m(n \cdot t_s) = \sum_{i=0}^{N_p-1} \sqrt{E_b} p(nt_s - iT_d - T_{RTT}) + v[n]\,;\, n = 0 \ldots N_p - 1 \tag{6.7}$$

The sample with index n corresponds to the $(i+1) - th$ pulse[1] if

$$0 \leq nt_s - iT_d - T_{RTT} \leq T_b \tag{6.8}$$

When (6.8) yields zero it is the first sample within the frame which corresponds to the pulse, i.e. the beginning of the pulse is sampled. If such sample has index n_k, the end of the pulse is sampled in the sample with index $n_k + N_s$. Moreover, the sampled signal will be the reconstructed pulse shape with a delay, n_k,which depends on the RTT. Thus we can rewrite (6.7) using a single pulse.

$$r_m[n] = \sqrt{E_b} p\left(n\frac{T_b}{N_s} - n_k\right) + v[n]\,;\, n = 0 \ldots N_p - 1 \tag{6.9}$$

Note that the resolution, $\frac{T_b}{N_s}$, is equivalent to the sampling rate used in the ideal UWB received described in section 2.2. Thus, the performance of the RTT measurement should be the same as the TOA estimation with $f_s = \frac{N_s}{T_b}$. However, the total error will be higher due to the pulse detection at the slave with UWB non-coherent receiver. The delay of the reconstructed pulse, n_k, is related to the RTT by

$$n_k = \frac{T_{RTT} N_s}{T_b} \tag{6.10}$$

Once the pulse is reconstructed, it is correlated with the known pulse shape as in the ideal receiver (section 2.2, see Figure 2.2). Hence, the delay can be estimated comparing the correlated signal with a threshold

[1]Note that $i = 0$ corresponds to the first pulse, that is why we write $(i+1) - th$ pulse

$$\sum_{n=n_0}^{n_0+N_s} r\left[n\right] p\left[n-n_0\right] \lessgtr \gamma \tag{6.11}$$

Where $p\left[n\right]$ is the pulse shape mask, which can be expressed as

$$p\left[n\right] = p\left(n\frac{T_b}{N_s}\right) \tag{6.12}$$

Then, the RTT is easily computed derived from (6.10)

$$\hat{T}_{RTT} = \frac{\hat{n}_k T_b}{N_s} \tag{6.13}$$

where $\hat{n}_k$ is the estimated delay of the reconstructed pulse in number of samples.

Chapter 7

Conclusions

Below is a brief list of conclusions that can be drawn from the results produced in this master thesis.

- The UWB non-coherent receivers based on the RTT measurement seem to be suitable for the distance measurement. The performance is worse than with the ideal receiver, but the loss is not big. The main advantage is the low complexity.
- Energy detection seems to present better performance regarding the accuracy, however, it requires higher SNR to work properly.
- Amplitude detection may be useful where it is not possible to have a high SNR. However, for long distances or large slave latency, the accuracy can get worse considerably.
- The slave latency is desirable to be as short possible in order to reduce the false alarm rate and therefore improve the accuracy, specially for amplitude detection since the accuracy is more affected than for energy detection.
- The proposed receiver based on undersampling may improve the performance of the non-coherent receivers, at the cost of requiring a more complex design and very accurate sampling rate. At the moment it seems to be difficult to implement, but it could be used as a start point in future works.

7.1 Discussion

7.1.1 Amplitude detection approach

The non-coherent receiver using the amplitude detection approach is very simple and the receiver front end only need to compare the signal with a threshold after the filtering and amplification. The main advantage of the amplitude detection approach is the low required SNR to achieve high probability of detection. On the other hand, the long distances (large propagation time) and mainly the slave latency make the accuracy to get worse considerably. Therefore, for low SNR and if the slave latency is not too long, it can be a good choice to use the amplitude detection approach.

7.1.2 Energy detection approach

The non-coherent receiver using the energy detection approach has also low complexity. It is more robust with long distances or large slave latencies. It requires a higher SNR to achieve a good probability of detection. Since which is compared with a threshold is the energy of the received signal, the noise is averaged and therefore the false alarm rate is lower, and therefore the accuracy is better.

7.1.3 UWB Pulse shapes

In the results of chapter 5, it has been shown that the main difference between the different shapes is for the detection performance, and mainly for amplitude detection (see Figures 5.3 and 5.4). For energy detection the difference between the shapes is negligible, while for amplitude detection the required SNR to achieve a certain detection performance is different for the different shapes. Particularly, Scholtz's monocycle presents the best detection performance. Therefore, such Scholtz's monocycle seems to be the best choice for UWB ranging systems due to its higher efficiency.

7.1.4 Amplitude detection vs energy detection

The design of both receivers is very similar. In energy detection approach, an energy detector is used instead of the comparator for amplitude detection (see chapter 4). Thus, regarding the complexity of the non-coherent receiver front end design, it does not seem that there is any preference between both approaches.

For short round-trip-times (considering also the slave latency), the amplitude detection approach seems to present better performance because to achieve a certain accuracy, lower SNR is required than with energy detection (selecting the threshold from the SNR to achieve a minimum detection performance). However, as the accuracy is more affected in amplitude detection when increasing the RTT, energy detection would present better performance for higher

RTTs. Since in practice the slave latency is quite long (it is actually several times higher than the propagation time), the energy detection approach is the best choice in general. Moreover, amplitude detection might be more robust in hostile environments where the SNR usually decrease because the detection performance changes slower with the SNR in amplitude detection than in energy detection (see 5.3 and 5.4).

7.1.5 UWB front end design

The design provided in this thesis is flexible and low-complex. Both amplitude detection and energy detection have been implemented. Due to lack of time, it has not been possible to perform experiments with the implemented boards and compare it with the simulations.

7.1.6 UWB receiver with undersampling

The proposed method to reconstruct a pulse from a burst of pulses using undersampling is an idea that could be used in the future. At the moment, it seems difficult to implement it because it requires very accurate sampling rate and pulses delay.

7.2 Future work

The simulations performed in this thesis are valid and can be useful to extract several conclusions. However, it probably won't match exactly the results of experiments. The reason is that the slave latency in practice is very long. In these simulations such slave latency has been considered zero or very short because otherwise the required time to perform each iteration of the simulations would have been increased considerably. Thus, a possible future work could be to carry out similar simulations, but with more realistic slave latency values.

Furthermore, as said before, it has not been possible to perform experiments because of time restriction and I had to come back to Spain three months ago, so during that time it was not possible. Hence, the next step of this thesis would to carry out the experiments with the implemented boards presented in chapter 4.

Another possible future work could be related to the signal processing part. An algorithm could be developed to adjust the threshold dynamically, setting a required probability of detection and increasing or decreasing the threshold to track such probability of detection. Thus, the accuracy would be the best which can be achieved for the given conditions.

The UWB receiver using undersampling, which is presented in chapter 6, could be used as a start point in future research. The method might be improved

to allow using the undersampling on both sides (master and slave). Variable delays within the pulse burst could also be considered.

The multipath characteristics of the UWB channels have not been considered in this thesis work. The UWB channels are actually highly dispersive, making that the leading-edge path is not necessarily the strongest path [18]. This is an issue to be further investigated in the context of UWB non-coherent receivers.

Bibliography

[1] A. De Angelis, S. Dwivedi and P. Händel, *"Characterization of a Flexible UWB Sensor for Indoor Localization".*

[2] H. Liu, H. Darabi, P. Banerjee, and J. Liu, "Survey of Wireless Indoor Positioning Techniques and Systems," *Systems, Man, and Cybernetics, Part C: Applications and Reviews, IEEE Transactions on*, vol. 37, no. 6, pp. 1067–1080, Nov. 2007.

[3] I. Skog, P. Händel, J. Nilsson, and J. Rantakokko, "Zero-velocity detection – an algorithm evaluation," *IEEE Transactions on Biomedical Engineering*, vol. 57, no. 11, pp. 2657–2666, Nov. 2010.

[4] D. Zachariah and M. Jansson, "Camera-aided inertial navigation using epipolar points," in *Position Location and Navigation Symposium* (PLANS), 2010 IEEE/ION, May 2010, pp. 303–309.

[5] B. Andò, S. Baglio, S. La Malfa, A. Pistorio, and C. Trigona, "A smart wireless sensor network for AAL," in IEEE International Workshop on Measurements and Networking Proceedings (M&N), Oct. 2011, pp. 122–125.

[6] J. Rantakokko, J. Rydell, P. Strömbäck, P. Händel, J. Callmer, D. Törnqvist, F. Gustafsson, M. Jobs, and M. Gruden, "Accurate and reliable soldier and first responder indoor positioning: multisensor systems and cooperative localization," *IEEE Wireless Communications*, vol. 18, no. 2, pp. 10–18, Apr. 2011.

[7] J. Rantakokko, P. Händel, M. Fredholm, and F. Marsten-Ekl ¨ of, "User requirements for localization and tracking technology: a survey of mission-specific needs and constraints," in *International Conference on Indoor Positioning and Indoor Navigation (IPIN)*, Zurich, Switzerland, September 14-17 2010.

[8] G. Santinelli, R. Giglietti, and A. Moschitta, "Self-calibrating indoor positioning system based on ZigBee R devices," in *IEEE Instrumentation and Measurement Technology Conference*, May 2009, pp. 1205–1210.

[9] D. Macii, F. Trenti, and P. Pivato, "A robust wireless proximity detection technique based on RSS and ToF measurements," in *IEEE International Workshop on Measurements and Networking Proceedings (M&N)*, Oct. 2011, pp. 31–36.

[10] A. De Angelis, M. Dionigi, R. Moschitta, A. Giglietti, and P. Carbone, "Characterization and Modeling of an Experimental UWB Pulse-Based Distance Measurement System," *IEEE Transactions on Instrumentation and Measurement*, vol. 58, no. 5, pp. 1479–1486, May 2009.

[11] Y. Zhou, C. L. Law, Y. L. Guan, and F. Chin, "Indoor elliptical localization based on asynchronous UWB Range measurement," *IEEE Transactions on Instrumentation and Measurement*, vol. 60, no. 1, pp. 248–257, Jan. 2011.

[12] S. Gezici and H. Poor, *"Position estimation via ultra-wide-band signals", Proceedings of the IEEE,* vol. 97, no. 2, pp. 386-403, 2009 .

[13] C. De Dominicis, A. Flammini, S. Rinaldi, E. Sisinni, A. Cazzorla, A. Moschitta, and P. Carbone, "High-precision UWB-based timestamping," in *International IEEE Symposium on Precision Clock Synchronization for Measurement Control and Communication (ISPCS)*, Sept. 2011, pp. 50–55.

[14] *Revision of part 15 of the commission's rules regarding ultra-wideband transmission systems*, Federal Communication Commission Std., 2002, Report and order, in FCC 02 48, Apr. 2002.

[15] *Electromagnetic compatibility and Radio spectrum Matters (ERM); Ultra WideBand (UWB) technologies for communication purposes;* ETSI EN 302 065, ETSI Std., Rev. V1.1.1, February 2008.

[16] A. De Angelis, J. Nilsson, I. Skog, P. Händel, and P. Carbone, "Indoor Positioning by Ultrawide Band Radio Aided Inertial Navigation," *Metrology and Measurement Systems*, vol. 17, no. 3, pp. 447–460, 2010.

[17] H. Wymeersch, J. Lien, and M. Win, "Cooperative localization in wireless networks," *Proceedings of the IEEE*, vol. 97, no. 2, pp. 427– 450, Feb. 2009.

[18] I. Guvenc and Z. Sahinoglu, "Threshold-Based TOA Estimation for Impulse Radio UWB Systems".

[19] I. Guvenc, Z. Sahinoglu, and P. V. Orlik, "TOA Estimation for IR-UWB Systems With Different Transceiver Types" in *IEEE Transactions on Microwave theory and techniques*, vol. 54, no. 4, April 2006.

[20] X. Chen and S. Kiaei, *"Monocycle Shapes for Ultra Wideband System".*

[21] H. Lee, B. Han, Y. Shin and S. Im, *"Multipath Characteristics of Impulse Radio Channels"*, Proceedings of the 1998 IEEE International Conference on Communications, ICC'98, vol.3, pp.1650-1654.

[22] H. Urkowitz, *"Energy Detection of Unknown Deterministic Signals", Proceedings of the IEEE*, vol 55, no 4, April 1967.

[23] D. Strömberg, A. De Angelis and P. Händel, "A low-complexity adaptive-threshold detector for pulse UWB systems," in *2011 International Workshop on ADC Modelling, Testing and Data Converter Analysis and Design and IEEE 2011 ADC Forum,* Orvieto, Italy, June 20 - July 1 2011.

[24] A. De Angelis, m. Dionigi, R. Giglietti and P. Carbone, "Experimental comparison of low-cost sub-nanosecond pulse generators," *IEEE Transactions on Instrumentation and Measurement*, vol. 60, no 1, pp. 310-318, Jan. 2011

[25] Freescale Semiconductor, MBC13720 Datasheet, Rev. 4, September 2011

[26] P. Withington, *"Impulse Radio Overview"*, Time Domain Corm.

[27] S. M. Kay, *"Fundamentals of Statistical Signal Processing Volume II",* Summary of Important PDF's

[28] M.K. Oh, B. Jong, R. Harjani, and D.J. Park, "A New Noncoherent UWB Impulse Radio Receiver" in *IEEE Communications Letters*, vol. 9, no. 2, February 2004.

[29] A. Mariani, A. Giorgetti, and M. Chiani, "Energy Detector Design for Cognitive Radio Applications" in *IEEE Invited paper*, 2010.

[30] K. Witrisal, G. Leus, G. J.M. Janssen, M. Pausini, F. Troesch, T. Zasowski, and J. Romme, "Noncoherent Ultra-Wideband Systems" in *IEEE Signal Processing Magazine*, July 2009.